Title

Actin filaments accumulate in the nucleus during interphase and remain in the vicinity of condensing chromosomes during prophase to metaphase in zebrafish early embryos

Haruka Oda[1], Yuko Sato[1], Shigehiro A. Kawashima[2], Yusuke Fujiwara[2], Máté Pálfy[3], Edlyn Wu[3,4], Nadine L. Vastenhouw[3,4], Motomu Kanai[2], and Hiroshi Kimura[1,*]

[1]Cell Biology Center, Institute of Innovative Research, Tokyo Institute of Technology, Yokohama 226-8503, Japan; [2]Graduate School of Pharmaceutical Sciences, The University of Tokyo, Tokyo 113-0033, Japan; [3]Max Planck Institute of Molecular Cell Biology and Genetics, Dresden-01307, Germany; [4]University of Lausanne, Center for Integrative Genomics, Lausanne 1015, Switzerland

Corresponding author: Hiroshi Kimura, hkimura@bio.titech.ac.jp

Key words

Nuclear actin, zebrafish embryo, live-cell imaging

Summary statement

Filamentous actin accumulates in the nucleus of zebrafish early embryos and forms patches associating with condensing chromosomes during prophase.

Abstract

In the cytoplasm, filamentous actin (F-actin) plays a critical role in cell regulation, including cell migration, stress fiber formation, and cytokinesis. Recent studies have shown that actin filaments that form in the nucleus are associated with diverse functions. Here, using live imaging of an F-actin-specific probe, superfolder GFP-tagged utrophin (UtrCH-sfGFP), we demonstrated the dynamics of nuclear actin in zebrafish (*Danio rerio*) embryos. In early zebrafish embryos up to around the high stage, UtrCH-sfGFP increasingly accumulated in nuclei during the interphase and reached a peak during the prophase. After nuclear envelope breakdown (NEBD), patches of UtrCH-sfGFP remained in the vicinity of condensing chromosomes during the prometaphase to metaphase. When zygotic transcription was inhibited by injecting α-amanitin, the nuclear accumulation of UtrCH-sfGFP was still observed at the sphere and dome stages, suggesting that zygotic transcription may induce a decrease in nuclear F-actin. The accumulation of F-actin in nuclei may contribute to proper mitotic progression of large cells with rapid cell cycles in zebrafish early embryos, by assisting in NEBD, chromosome congression, and/or spindle assembly.

37 **Introduction**

38 Actin is a highly conserved protein throughout eukaryotes. In the cytoplasm, actin
39 serves a role in cell migration, stress fiber formation, and cell division by forming a
40 contractile ring during cytokinesis. Actin is also present in nuclei, where it plays a crucial
41 role in transcriptional regulation (Vartiainen *et al*., 2007; Baarlink *et al*., 2013; Tian *et al*.,
42 2016; Sokolova *et al*., 2018) and in DNA damage repair processes (Chiolo *et al*., 2011;
43 Belin *et al*., 2015; Caridi *et al.*, 2019). Actin nuclear localization is mediated through the
44 interplay of nuclear import regulated by importin 9 with cofilin (Dopie *et al*., 2012) and
45 nuclear export regulated by exportin 6 (Exp6), which transports profilin-actin complexes
46 (Stüven *et al*., 2003). Whereas filamentous actin (F-actin) is rarely observed in somatic
47 cell nuclei, it is presumed to be involved in regulating the function and structure of
48 undifferentiated cell nuclei (Misu *et al.*, 2017).

49 In mouse early embryonic nuclei, F-actin facilitates nuclear expansion during the G1
50 phase (Baarlink *et al*., 2017) and maintains the integrity of the totipotent state of the cell
51 mass (Okuno *et al.*, 2020). Nuclear actin polymerization via Wave-1 is required for
52 reprogramming somatic nuclei that are transplanted into African clawed frog (*Xenopus*
53 *laevis*) oocytes (Miyamoto *et al*., 2011). Actin has a distinct role in the large nucleus of
54 oocytes, which is also called the germinal vesicle (GV). *Xenopus laevis* GV contains a
55 high concentration of actin to maintain the large nuclear structure (Clark and Merriam,
56 1977; Clark and Rosenbaum, 1979; Bohnsack *et al*., 2006). In mammalian oocytes, F-
57 actin bundle in GVs stabilizes the chromatin mobility and secures the accurate
58 chromosome alignment and segregation (Mogessie and Schuh, 2017; Scheffler *et al.*,
59 2022; Dunkley *et al.*, 2022). In starfish oocytes, actin mesh forms in the nuclear area
60 after nuclear envelope break down (NEBD; Lénárt *et al*., 2005), and the contraction of

61 the actin meshwork transports chromosomes until they are captured by microtubules
62 (Mori *et al*., 2011). In addition, F-actin polymerizes underneath the nuclear envelope and
63 accelerates fragmentation of the nuclear envelope during the first stage of NEBD (Mori
64 *et al*., 2014; Wesolowska *et al*., 2020).

65 During *Xenopus* embryonic development, F-actin accumulates in nuclei up to the
66 blastula stage, when the major wave of zygotic transcription begins, before diminishing
67 at the gastrula stage (Oda *et al*., 2017). A reconstituted system utilizing *Xenopus* egg
68 extracts has been used for analyzing the assembly of early embryonic nuclei from de-
69 membraned sperm *in vitro* (Murray, 1991). In reconstituted nuclei using this system,
70 nuclear actin prevents chromatin aggregation during interphase and facilitates
71 chromosome alignment during prometaphase (Oda *et al*., 2017). However, the dynamics
72 of nuclear actin during *Xenopus* embryo development have not been elucidated,
73 because live-cell imaging is hampered by the melanin granules that are present in the
74 cortex of embryos.

75 In contrast to the African clawed frog (*Xenopus laevis*), zebrafish (*Danio rerio*) embryos
76 that share a similar developmental process with frog are transparent and thus suitable
77 for live-cell imaging. During the early embryo stages of zebrafish, cells have relatively
78 large nuclei and undergo a series of short and synchronized cell cycles without
79 transcription and gap phases (Satoh, 1977; Kimmel *et al*., 1995; Joseph *et al*., 2017),
80 which also occurs in *Xenopus* embryos (Jevtić and Levy, 2015; Newport and Kirschner,
81 1982; Lucas *et al*., 2000; Mahbubani *et al*., 1992).

82 In zebrafish embryos, transcription from the zygotic gene is observed as early as at the
83 64-cell stage, and becomes further activated at around the 512-cell to 1k-cell stages
84 (Mathavan *et al*., 2005; Heyn *et al*., 2014; White *et al*., 2017; Pálfy *et al*., 2017;

85 Vastenhouw *et al*., 2019). After the 1k-cell stage, the cell cycle elongates and loses
86 synchronicity, which occurs with the onset of differentiation (Kane *et al*., 1992).
87 Fluorescently labeled phalloidin has been the standard reagent to stain F-actin in fixed
88 cells (Dancker *et al*., 1975; Wehland *et al*., 1977). Live-cell actin-specific probes have
89 also been developed, including fluorescent protein-tagged LifeAct and UtrCH, as well as
90 actin-specific chromobody (Actin-chromobody®, Rocchetti *et al*., 2014). UtrCH, which is
91 the Calponin Homology domain of human utrophin (Burkel *et al*., 2007), is an actin-
92 binding peptide that is more selective to F-actin than LifeAct, which is derived from the
93 yeast actin-binding protein, Abp140 (Riedl *et al*., 2008). In this report, we mainly used
94 superfolder GFP-tagged UtrCH (UtrCH-sfGFP) to track nuclear F-actin dynamics in
95 zebrafish early embryos. We observed that F-actin accumulates in nuclei during
96 interphase and the actin patches remained in the vicinity of condensing chromosomes
97 during the prophase to metaphase.

98 **Results**

99 **Visualizing nuclear F-actin in zebrafish early embryos**

100 To investigate whether F-actin accumulates in nuclei in zebrafish early embryos, we
101 first aimed to detect F-actin by using fixed embryos stained with fluorescently labeled
102 phalloidin. DNA was counterstained with Hoechst dye. Phalloidin signals were enriched
103 in nuclei in the 32-, 128-, and 1k-cell stages, particularly in Hoechst-poor regions (Fig.
104 1A-C). In the sphere stage embryos, the total nuclear phallodin signals were decreased
105 whereas filamentous structures were observed (Fig. 1B and 1C). This observation
106 suggests that F-actin is abundantly present in nucleoplasm during the early stages of
107 zebrafish development, as was observed in *Xenopus laevis* embryos (Oda *et al*., 2017).
108 Although the filamentous structures observed at the later stages are of interest, we here
109 focused on the dynamics and function of nuclear F-actin that are abundantly
110 accumulated at the earlier stages.

111 To visualize nuclear F-actin dynamics in living zebrafish embryos, purified UtrCH-sfGFP
112 (Fig. S1A) was injected into the yolk of 1-cell stage embryos. The antigen-binding
113 fragment (Fab) specific for acetylation of histone H3 lysine 9 (H3K9ac), which distributes
114 throughout the chromatin from the early stage of development, labeled with Cy5 was co-
115 injected as a chromatin marker (Sato *et al.*, 2019). The injected embryos were set onto
116 a confocal microscope at the 4-cell stage, and three-dimensional time-lapse images were
117 acquired every 90 s from the 8-cell stage to the oblong stage. UtrCH-sfGFP signal is
118 enriched in the interphase nuclei of embryos from the 8-cell stage to the 1k-cell stage
119 (Fig. 1D, arrowheads and insets; Fig. 2A; Movie 1). At the oblong stage (3.5 hours post-
120 fertilization; hpf), UtrCH signals in nuclei became weaker compared to those in earlier
121 stages (Figs. 1D). These live-cell imaging data are consistent with the observations in

122 fixed embryos.

123 Time-laps imaging with 1.5-min intervals (Fig. 2A and Fig. S2) and measurements of
124 the nucleus to the cytoplasm intensity ratio (N/C ratio) of UtrCH-sfGFP (Fig. 2B) revealed
125 that UtrCH-sfGFP signal began to accumulate in the nucleus at the end of telophase,
126 and became more concentrated during interphase, peaking just before mitosis, and then
127 disappeared from mitotic chromosome areas during 16-cell to 1k-cell stages. After the
128 1k-cell stage, the mean value of UtrCH-sfGFP N/C ratio reduced to less than 1.0 (Fig.
129 2B).

130 Because UtrCH could stabilize actin filaments and influence actin dynamics (Spracklen
131 *et al*., 2014), we used another actin-binding peptide, LifeAct, which binds to globular actin
132 (G-actin) and F-actin (Riedl *et al*., 2008), as the sfGFP-tagged version (LifeAct-sfGFP)
133 to validate the results obtained with UtrCH (Fig. 2). Purified LifeAct-sfGFP (Fig. S1B)
134 was co-injected with Cy3-labeled anti-phosphorylated histone H3 serine 28 (H3S28ph)
135 Fab to highlight chromosomes from the prometaphase to anaphase (Hayashi-Takanaka
136 *et al*., 2014) and Cy5-labeled anti-H3K9ac Fab to label nuclei (Fig. S1C). LifeAct-sfGFP
137 was concentrated in nuclei, showing >1.0 N/C ratio, during early embryonic stages (Fig.
138 3). After the 1k-cell stage, the LifeAct-sfGFP N/C ratio reduced to <1.0 (Fig. 3B), as was
139 observed in UtrCH-sfGFP (Fig. 2B). This lowered N/C ratio on average could be
140 attributed to the less nuclear accumulation and/or the asynchronized cell cycle, as cells
141 in the mitotic phase showed a low N/C ratio (Figs. 2 and 3).

142 We then analyzed N/C ratios in individual interphase nuclei by eliminating H3S28ph-
143 positive mitotic cells (Fig. 3C). The cumulative bar chart showed that >90% of interphase
144 nuclei exhibited a LifeAct-sfGFP N/C ratio >1.0 up to the 256-cell stage. At the 512- and
145 1k-cell stages, the fraction of nuclei with an N/C ratio of >1.0 decreased to ~80% and

146 ~65%, respectively (Fig. 3C). After the 1k-cell stage, the fraction of nuclei with an N/C
147 ratio of <1 increased substantially (Fig. 3C, 150 min), reaching ~90% at the sphere (180
148 min) and dome (195 min) stages. Taken together with the phalloidin-staining and UtrCH-
149 sfGFP data, these results suggest that actin is gradually concentrated and polymerized
150 in nuclei during the interphase in the early stages of zebrafish embryos, as observed in
151 *Xenopus* (Oda *et al.*, 2017), and the amount of nuclear actin decreases after the 1k-cell
152 stage.
153
154 **F-actin accumulates in the nucleus during interphase to prophase and remains**
155 **along with condensing chromosomes during early prometaphase**
156 Since nuclear UtrCH-sfGFP reached a peak just before mitosis (Fig. 2A, 7.5, 9.0, and
157 10.5 min; Fig. S2A, 7.5, 9.0, and 10.5 min, 3A, 10.5 min), we investigated F-actin
158 dynamics during the late interphase to mitosis in detail. For this purpose,
159 tetramethylrhodamine-labeled 155-kDa dextran (TMR-dextran) was used for monitoring
160 the timing of NEBD; TMR-dextran that was injected into the cytoplasm cannot enter to
161 the nucleus due to its big size until the nuclear membrane breaks down at the onset of
162 prometaphase. Thus, NEBD was identified by the onset of TMR-dextran leakage into the
163 nucleus. In addition, we used JF646-labeled latency-associated nuclear antigen peptide
164 (JF646-LANA) to track chromatin throughout the cell cycle. The LANA peptide binds to
165 the acidic patch in the nucleosome (Barbera *et al.*, 2006), and a synthetic LANA peptide
166 with polyethylene glycol and fluorescein was shown to label chromatin in living cells
167 (Fujiwara *et al.*, 2021). In the current study, JF646-LANA was synthesized (see Materials
168 and methods) to be used together with sfGFP- and TMR/Cy3-labeled probes. Mitotic
169 chromosomes visualized with Cy3-H3S28ph Fab were indeed more intensely detected

170 by JF646-LANA than by H3K9ac Fab, whose chromatin binding is decreased by
171 deacetylation during mitosis (Fig. S1C and S1D).

172 To visualize F-actin dynamics at around NEBD, 1-cell stage embryos were injected with
173 UtrCH-sfGFP, TMR-dextran, and JF646-LANA, and were imaged every 12.5 s from 256-
174 cell stage. Figure 4 shows the representative images of cells in the 1k-cell stage (A) and
175 high stage (B) embryos with the changes in N/C intensity ratio of UtrCH-sfGFP and TMR-
176 dextran (C). UtrCH-sfGFP accumulated in nuclei (Fig. 4, −37.5 s to −12.5 s), reaching a
177 peak concomitantly with NEBD as indicated by TMR-dextran diffusing into nuclear areas
178 (Fig. 4, 0 s). After NEBD, UtrCH signals were remained in the vicinity of condensing
179 chromosomes during prometaphase (Fig. 4, 0 s to 25 s), and almost disappeared from
180 the chromosome areas by metaphase (Fig. 4, 37.5 s).

181 To track microtubule dynamics with F-actin and chromosomes during prophase to
182 metaphase, TMR-labeled tubulin was co-injected with UtrCH-sfGFP and JF646-LANA,
183 and three-dimensional images were acquired every 15 s at the 256-cell (Movie 2), 512-
184 cell (Movie 3), 1k-cell (Fig. 5 and Movie 4), high (Fig. 6 and Movie 5), sphere (Fig. 7),
185 and dome stages (Fig. S3). UtrCH-sfGFP was located in the nucleus with enrichment at
186 around the nuclear periphery of the 1k-cell stage embryo before NEBD (Fig. 5, −15 s).
187 Just after NEBD, UtrCH-sfGFP remained in the vicinity of the condensing chromosomes,
188 and microtubule spindles (TMR-Tubulin) grown from centrosomes extended along with
189 the chromosomes (Fig. 5A, 0 s and 15 s; see also Fig. 5B for 3D rendering views). UtrCH-
190 sfGFP signals gradually disappeared from the nuclear areas during prometaphase to
191 metaphase (Fig. 5A, 30–45 s; and Fig. 5B, 30 s). Concomitantly with actin diminishment,
192 microtubule spindles appeared to capture chromosomes for their segregation (Fig. 5, 45
193 s to 90 s). Similar dynamics of actin and tubulin were observed from the 256-cell stage

194 to 1k-cell stages (256-cell stage: Movie 2, 512 cell-stage: Movie 3). In the oblong stage,
195 the UtrCH-sfGFP signal in the nucleus was much weaker (Fig. 6, −45s to 0 s); however,
196 after the NEBD, the actin patches were still observed in the vicinity of condensing
197 chromosomes (Fig. 6, 15 s and 30 s). In the sphere stage, the timing of UtrCH-sfGFP
198 nuclear accumulation was more transient and the signals were much weaker than those
199 during the 1k-cell stage (Fig. 7, 0 s and 15 s). Only a trace amount of UtrCH-sfGFP was
200 observed in the chromosome area in the dome stage Fig. S3, 30 s and 45 s).
201
202 **Transcription inhibition prolonged nuclear actin decrease after zygotic genome**
203 **activation (ZGA)**
204 We next examined the relationship between zygotic transcription and nuclear F-actin,
205 because the amount of F-actin was substantially decreased after the oblong stage, as in
206 most somatic cells (Schoenenberger *et al*., 2005; Hofmann *et al*., 2009; Xu *et al*., 2010;
207 Parisis *et al*., 2017). To test whether zygotic transcription is required to diminish nuclear
208 F-actin, we injected α-amanitin, which directly binds to RNA polymerase II and interferes
209 with its translocation and nucleotide incorporation (Nguyen *et al*., 1996; Brueckner and
210 Cramer, 2008), into zebrafish embryos (Fig. 8A; Kane *et al.*, 1996; Sato *et al.*, 2019).
211 Embryos that were injected with α-amanitin or the buffer were fixed at the 1k-cell and
212 oblong stages and stained with Hoechst and phalloidin. In 1k-cell stage embryos, in
213 which major ZGA typically begins, phalloidin signals were concentrated in the nuclei,
214 regardless of α-amanitin injection (Fig.8B, 1k-cell). In contrast, at the oblong stage,
215 nuclear phalloidin signals were slightly enriched in α-amanitin-injected embryos
216 compared to those detected in the control embryos (Fig. 8B, oblong). We then confirmed
217 the effect of α-amanitin on nuclear F-actin in living cells by using UtrCH-sfGFP. In the

218 both amanitin-treated and control embryos, the N/C ratio of UtrCH-sfGFP began to
219 decrease after the high stage (Fig. 8C). However, compared to the control, the N/C ratio
220 in α-amanitin-injected embryos remained relatively high at sphere and dome stages (Fig.
221 8C). These data suggest that the decrease of the N/C ratio of UtrCH-sfGFP is facilitated
222 by zygotic transcription.
223
224 **Attempts to disturb nuclear actin in zebrafish early embryos.**
225 To investigate the physiological role of nuclear F-actin in early embryos, we sought to
226 artificially manipulate its levels. The first attempt to decrease nuclear actin by ectopic
227 expression of Exp6, which is known to export actin from the nucleus to the cytoplasm
228 (Stüven *et al*., 2003), by injecting mRNA encoding 3×FLAG-tagged zebrafish Exp6 into
229 embryos. However, Exp6-3×FLAG expression induced severe cytokinesis defects but
230 did not decrease nuclear actin levels (Fig. S4).
231 Next, we expressed a polymerization-deficient actin mutant (R62D), in which Arg 62
232 was substituted to Asp (Posern *et al*., 2002), tagged with the superfolder Cherry and a
233 nuclear localizing signal (Actin R62D-sfCherry-NLS), to inhibit nuclear F-actin formation.
234 The wild type actin tagged with sfCherry-NLS (Actin WT-sfCherry-NLS) and sfCherry-
235 NLS were used as controls to examine the effect of the wild-type actin and sfCherry
236 alone. Embryos were co-injected with mRNA encoding Actin R62D-sfCherry-NLS, Actin
237 WT-sfCherry-NLS, or sfCherry-NLS, with UtrCH-sfGFP and Cy5-labeled H3K9ac-
238 specific Fab and were imaged from 8-cell stage. The N/C intensity ratios of UtrCH-sfGFP,
239 however, did not show obvious differences among embryos expressing sfCherry-NLS,
240 Actin R62D-sfCherry-NLS, and Actin WT-sfCherry-NLS (Fig. S5A and S5B). Expression
241 of Actin R62D tagged with smaller 3xFLAG tagged versions, instead of sfCherry, also did

242 not affect the N/C ratios of UtrCH-sfGFP (Fig. S5C). Because actin was already
243 abundantly present in nuclei, additional expression of the wild-type or mutant actin might
244 have minimal effects.
245 In has been reported that cofilin proteins actively depolymerize actin filaments in
246 cytoplasm during the interphase (Vartiainen *et al*., 2002; Amano *et al*., 2002; Kaji *et al*.,
247 2008; Chin *et al*., 2016; Wioland *et al*., 2017). Cofilin1 is the non-muscle isoform
248 expressed ubiquitously while cofilin2 is the muscle isoform. We expressed zebrafish
249 cofilin1 and cofilin2, tagged with sfCherry and an NLS, to attempt depolymerizing nuclear
250 actin in embryos, but again the N/C intensity ratios of UtrCH-sfGFP were not affected
251 (Fig. S6). Thus, it was not possible to manipulate the level of nuclear F-actin in our
252 experimental conditions. Nuclear F-actin level might be robustly regulated in zebrafish
253 early embryos.
254
255 **Discussion**
256 **Nuclear actin accumulation in zebrafish early embryos**
257 We demonstrated F-actin accumulation in zebrafish early embryo nuclei by fixed cells
258 using phalloidin and by living cells using fluorescent actin-binding probes. In living
259 embryos from the 8-cell to 1k-cell stages, UtrCH-sfGFP, which selectively binds to F-
260 actin, gradually accumulated in the nucleus during the interphase, thereby reaching the
261 maximum amount at around NEBD. After the high stage, UtrCH-sfGFP was not much
262 concentrated in nuclei, while some filamentous structures were more evidently observed.
263 These data are consistent with previous findings in mouse and *Xenopus laevis* early
264 embryos (Baarlink *et al*., 2017; Oda *et al*., 2017), which indicates that nuclear F-actin
265 accumulation in undifferentiated cells is common in vertebrates (Xu *et al*., 2010;

266 Miyamoto *et al.*, 2011; Miyamoto *et al*., 2013; Sokolova *et al*., 2018; Okuno *et al*., 2020).
267 After ZGA, the level of nuclear F-actin drops. The decrease appears to be induced by
268 zygotic transcription, as nuclear F-actin was still observed in the sphere-stage embryos
269 that were treated with α-amanitin, an RNA polymerase II inhibitor. Maternal-to-zygotic
270 transition may alter the balance of nuclear import and export factors of actin, as it was
271 previously demonstrated that the actin exporter, Exp6, is not expressed in *Xenopus*
272 oocytes nor in early embryonic stages, yet it becomes expressed after ZGA (Bohnsack
273 *et al*., 2006).
274
275 **Nuclear F-actin may facilitate chromosome congression and regulate microtubule**
276 **growth**
277 In early-stage zebrafish embryos, the peak of nuclear F-actin accumulation was
278 concurrent with the timing of NEBD and F-actin localized in the vicinity of condensing
279 chromosomes during prometaphase before disappearing during metaphase. This actin
280 behavior is similar to that observed in starfish oocytes (Lénárt *et al*., 2005; Mori *et al*.,
281 2011; Mori *et al*., 2014; Wesolowska *et al*., 2020). In starfish oocyte GV, F-actin is
282 assembled underneath the nuclear membrane and forms spikes toward to the nuclear
283 membranes, which contribute to membrane rupture and NEBD (Mori *et al*., 2014;
284 Wesolowska *et al*., 2020). After the germinal vesicle breakdown, actin meshwork catches
285 chromosomes and shrinks like a fishnet to transport them over a long distance toward
286 underneath the starfish oocyte cortex in meiosis II (Lénárt *et al*., 2005; Mori *et al*., 2011).
287 In the mouse oocyte, both nuclear F-actin and spindle F- actin protect the chromosomes
288 misalignment and missegregation at the meiosis (Mogessie and Schuh, 2017; Scheffler
289 et al., 2022). It is interesting to speculate that the function of actin in large oocyte cells

290 may partially be retained in fertilized eggs, although it is unknown whether a similar
291 system to starfish is conserved in zebrafish oocytes. During the short cell cycle of
292 zebrafish embryos, the spindle checkpoint is weak until the zygotic genome activation
293 (Ikegami *et al*., 1997). In relatively large cells during the early embryonic stages, actin
294 patches remained around chromosomes may assist in chromosome congression, just as
295 the actin meshwork in starfish oocytes. It is also possible that actin patches guide
296 microtubule assembly and promote proper and rapid spindle formation, as recent reports
297 have shown that actin supports proper spindle formation in *Xenopus* gastrula embryos,
298 mouse and human oocytes, and cultured cells (Woolner *et al*., 2008; Mogessie and
299 Schuh, 2017; Roeles and Tsiavaliaris, 2019; Plessner *et al*., 2019; Farina *et al*., 2016;
300 Farina *et al*., 2019; Kita *et al*., 2019). However, “spindle-actin” has been depicted with
301 barrel structures composed of fine actin fiber at metaphase, unlike actin patches during
302 the prometaphase of zebrafish embryos. We speculate that the accumulation of F-actin
303 in nuclei in zebrafish early embryos contribute to proper mitotic progression by assisting
304 in NEBD, chromosome congression, and/or spindle assembly under rapid cell cycles
305 with weak checkpoint mechanism.
306
307 **Manipulation of nuclear actin level in zebrafish embryos**
308 We took different approaches to decrease the level of nuclear F-actin by expressing
309 Exp6, an NLS-tagged Actin R62D, and NLS-tagged cofilin; unfortunately, however, none
310 of them were successful. Exp 6 and NLS-tagged Actin R62D have been used to decrease
311 nuclear actin and inhibition of nuclear actin polymerization, respectively, in previous
312 reports (Bohnsack *et al*., 2006; Okuno *et al*., 2020; Miyamoto *et al*., 2011; Spencer *et al*.,
313 2011; Dopie *et al*., 2012; Parisis *et al*., 2017; Baarlink *et al*., 2017). However, we did not

314 observe significant decreases of UtrCH-sfGFP N/C ratios in zebrafish embryos
315 expressing Exp6 and Actin R62D, under the conditions that did not affect cytoplasmic F-
316 actin. Increasing the expression levels of those proteins by injecting more mRNA affected
317 cytoplasmic F-actin causing defects in cytokinesis. We also attempted to decrease
318 nuclear F-actin using NLS-tagged cofilin 1 and cofilin 2, which are actin-depolymerizing
319 factors (Amano *et al*., 2002; Vartiainen *et al*., 2002; Kaji *et al*., 2008; Chin *et al*., 2016;
320 Wioland *et al*., 2017); however, their expression did not affect nuclear F-actin levels. In
321 addition, the expression of NLS-tagged wild-type actin did not increase UtrCH-sfGFP
322 N/C ratio. It can be speculated that nuclear actin is very abundant and the ectopic wild-
323 type actin or R62D mutant may not affect much on the total F-actin level. Also, F-actin
324 formation in the nucleus may be robustly regulated, and expressing factors that assist in
325 actin depolymerization may be compensated when the expression level is mild not
326 affecting the cytoplasmic actin.
327

328 **Materials and methods**

329 **Zebrafish embryo preparation for live imaging**

330 To obtain fertilized eggs, 5–10 pairs of AB line WT zebrafish (*Danio rerio*) males and
331 females were crossed. Embryos were dechorionated using 1 mg/mL pronase
332 from *Streptomyces griseus* (SIGMA, 10165921001) diluted in 0.3× Danieau's buffer
333 [17.4 mM NaCl, 210 μM KCl, 120 μM $MgSO_4$, 180 μM $Ca(NO_3)_2$, 1.5 mM HEPES, pH
334 7.6]. For actin visualization, UtrCH-sfGFP (1.46 fmol; see below) or LifeAct-sfGFP (2.3
335 fmol; see below) was injected with labeled Fabs (anti-H3K9ac [CMA315; 50 pg], anti-
336 H3S28ph [CMA315; 50 pg]; anti-DYKDDDDK tag [FUJIFILM Wako, 012-22384; 50 pg];
337 Sato *et al*., 2019) and 10 fmol JF646-LANA (see below) in 0.5 nL phosphate-buffered

338 saline (PBS, Takara, T900) containing 0.05% phenol red (SIGMA, P5530) as an injection
339 marker, were injected into the yolk of 1-cell stage embryos. For NEBD or tubulin
340 visualization, TMR-labeled 155-kDa dextran (250 pg in 0.5 nL PBS, SIGMA, T1287) or
341 TMR-labeled tubulin (1.25 ng in 0.5 nL General Tubulin Buffer, Cytoskeleton, TL590M)
342 was injected with UtrCH-sfGFP and JF646 LANA. When mRNA was also injected, mRNA
343 of sfCherry-NLS or 3×FLAG-tagged Actin WT or R62D (125 pg in 0.5 nL water), 3×FLAG-
344 tagged Exp6 (150 pg in 0.5 nL water), sfCherry-NLS-tagged cofilin1 (125 or 400 pg in
345 0.5 nL water) or sfCherry-NLS-tagged cofilin2 (125 pg in 0.5 nL water) was first injected
346 into the cell of 1-cell stage embryos, and then UtrCH-sfGFP, LifeAct-sfGFP, Fabs, and/or
347 JF646-LANA were injected into the yolk. For transcription inhibition, 250 pg α-amanitin
348 (Merck, 129741) in 0.5 nL PBS was injected into the yolk of 1-cell stage embryos (Kane
349 *et al*., 1996; Sato *et al*., 2019). To monitor the transcription inhibition, 530 pg of Cy3-
350 labeled antisense morpholino oligonucleotide specific to miR-430 transcripts (Hadzhiev
351 *et al*., 2019) in 0.5 nL water was injected into the yolk of the 1-cell stage embryos with
352 JF646-LANA. The injected embryos were incubated at ~25°C up to the 4-cell stage and
353 embedded into 0.5% agarose type VII-A low melting temperature (SIGMA, A-0701) in
354 PBS on a glass bottom dish (IWAKI, 3791-035) with the animal pole positioned down for
355 live-cell imaging.
356 All zebrafish experiments were approved by the Tokyo Institute of Technology Genetic
357 Experiment Safety Committee (I2018001), and animal handling was carried out
358 according to the guidelines.
359
360 **Zebrafish embryo fixation and staining**
361 For Fig. 1A and B, dechorionated embryos were incubated until fixation at the desired

362 stage with 4% paraformaldehyde in 250 mM HEPES for 3 h at 25°C. After fixation,
363 embryos were washed three times with PBS and stained with 2 μg/mL Hoechst 33342
364 (Nacalai Tesque, 04929-82) and 20 nM Acti-stain™ 555 phalloidin (Cytoskeleton,
365 PHDH1-A) in PBS containing 0.05% Triton X-100 at 4°C overnight in the dark. Stained
366 embryos were washed three times with PBS before microscopic observation. For Fig.
367 8B, embryos were injected with α-amanitin (250 pg in 0.5 nL) or PBS (0.5 nL) as the
368 control and incubated until the 1k-cell or oblong stage and fixed with 4%
369 paraformaldehyde in 250 mM HEPES for 3 h at 25°C. After the fixation, embryos were
370 washed with PBS and embedded in 100 μL 0.5% agarose in PBS and covered with 100
371 μL 1% agarose to prevent the detachment of embryos from a glass bottom dish. Embryos
372 were stained with 2 μg/mL Hoechst 33342 and 20 nM Acti-stain™ 555 phalloidin in PBS
373 containing 0.05% Triton X-100 in the dark with gentle shaking (Titec, Shake-XR; 40 rpm)
374 overnight. Stained embryos were washed three times with PBS before microscopic
375 observation.

376 **Embryo imaging**

377 Images were collected using a confocal microscope. For Figs. 1, 2, 3, 8A, 8C, S2, S4,
378 S5, S6, and Movie 1, images were acquired using a confocal microscope FV1000
379 (OLYMPUS) operated under built-in software (FLUOVIEW-ASW, version 4.2) with a
380 UPLSAPO 30× silicone-immersion objective lens (NA 1.05), with 150 μm pinhole, zoom
381 1.0×, and 488-nm, 543-nm, and 633-nm laser lines on a heated stage at 28°C (Tokai Hit).
382 For live imaging of Figs. 1D, 2A, 3A, 8C, S2, S4, S5, S6, and Movie 1, 25 z-stack images
383 (4 μm z-intervals; 512 × 512 pixels) were taken with 90 s intervals.
384 For high-speed or higher resolution imaging to produce the images shown in Figs. 4, 5,
385 6, 7, 8A, S1C, S1D, S3, and Movie 2–5, images were taken using a spinning disk

386 confocal system consisting of an inverted microscope (Ti-E, Nikon) with an Apo 40×
387 water-immersion objective lens (NA 1.25; Figs. 4, 5, 6, 7, 8A, S3 and Movies 2–5) or a
388 Plan Apo 25× silicon-immersion objective lens (NA 1.05, Fig. S1C and S1D), a spinning
389 disk unit with 40 μm pinhole (Dragonfly, Oxford Instruments), a laser unit with 488-nm,
390 561-nm and, 637-nm laser lines, and an EM-CCD camera (iXon Life 888, Oxford
391 Instruments), operated under Fusion software (version 2.0 and 2.2, Oxford Instruments).
392 15–25 z-stack images (1, 2, or 4 μm z-intervals; 1024 × 1024 pixels) were taken with
393 12.5, 15, 60, or 90 s time intervals at 25°C.

394 **Actin-binding peptides**

395 DNA fragment encoding UtrCH (1-262 of human utrophin, NM_007124) or LifeAct (Riedl
396 *et al*., 2008) gifted from Dr. Mari Iwabuchi (Nagoya University, Japan) was fused with the
397 sfGFP gene with a linker sequence (DPPVAT) and was cloned into a pGEX6P-1 vector
398 that has the N-terminal glutathione S-transferase (GST) tag (Cytiva). *E. coli* BL21 (DE3)
399 cells harboring the pGEX6P-1-based expression plasmid were grown in 24 mL Plusgrow
400 II (Nacalai Tesque, 08246-86) medium overnight at 25°C. The overnight culture (24 mL)
401 was diluted into 400 mL PlusgrowII medium and further incubated at 25°C for 3 h. The
402 expression of GST-UtrCH-sfGFP and GST-LifeAct-sfGFP was induced in *E. coli* BL21
403 (DE3) at 25°C for 7 h by adding 1 mM isopropyl β-D-thiogalactopyranoside (Nacalai
404 Tesque, 19742-94). Harvested bacterial cells (400 mL, 4,000 ×*g*, 10 min, 4°C) were
405 suspended in 20 mL ice-cold 50 mM Tris–HCl (pH 7.4) buffer containing 1 mg/mL
406 lysozyme (Seikagaku Corporation, 100940) and 1× protease inhibitor cocktail (Nacalai
407 Tesque, 03969-21) and were lysed by sonication (Branson; SONIFIRE 250; output
408 control: 1, duty cycle: 50% for 2 min repeated 14 cycles with 30 s interval) in an ice bath.
409 Triton X-100 (10% in water) was added to the sonicated solution to yield the final

410 concentration at 1% and the mixture was incubated for 30 min at room temperature with
411 a gentle rotation (Titec, RT-50; 30 rpm). After centrifugation (10,000 ×*g* for 20 min at 4°C),
412 the supernatant was mixed with 5 mL (bed volume) glutathione sepharose 4B beads
413 (Cytiva, 17075605; prewashed with PBS) and gently rotated (Titec, RT-50; 30 rpm) at
414 4°C for 20 h in the dark. The beads were collected in a Poly-Prep® Chromatography
415 Columns (BioRad) and washed with a 10-column volume of PBS. GST-UtrCH-sfGFP or
416 GST-LifeAct-sfGFP was eluted using a 5-column volume of 10 mM glutathione
417 (FUJIFILM Wako Pure Chemical, 073-02013) containing 50 mM Tris–HCl (pH 8.7). The
418 eluate was concentrated down to 1.5 mL using an Amicon Ultra Centrifuge Filter unit (30
419 kDa cutoff for GST-UtrCH-sfGFP and 10 kDa cutoff for GST-LifeAct-sfGFP; Merck,
420 UFC903024 and UFC901024, respectively). The GST tag was removed by digestion with
421 8 units/mL PreScission Protease (Cytiva, 27084301) on ice for 24–36 h and then
422 removed through glutathione sepharose 4B beads (5 mL bed volume) packed twice in
423 Poly-Prep® Chromatography Columns (BioRad). UtrCH-sfGFP and LifeAct-sfGFP were
424 further purified through gel filtration column chromatography (HiLoad 16/600 Superdex
425 75 pg, Cytiva, 28989333) using AKTAPrime™PLUS (Cytiva, 11001313). After loading
426 1.5 ml of the protein sample, 30 mL fractions were collected and analyzed by 15%
427 sodium dodecyl sulfate (SDS)-polyacrylamide gel electrophoresis (SuperSep Ace,
428 FUJIFILM Wako Pure Chemical, 190-15001). The highly pure fractions were collected
429 (Supplementary Fig. S1A and S1B), aliquoted, snap-frozen in liquid N_2, and stored at
430 −80°C. Once thawed, recombinant proteins were stable at 4°C for at least 5 days.
431
432 **Fab preparation**
433 Dye-conjugated Fabs were prepared as previously described (Kimura and Yamagata,

434 2015). In brief, 100 μg purified Fab (anti-H3K9ac: CMA310/19E5, Hayashi-Takanaka *et*
435 *al*., 2011; anti-H3S28ph: CMA315/10-20F11, Hayashi-Takanaka *et al*., 2014; anti-
436 DYKDDDDK tag: FUJIFILM Wako, 012-22384) was reacted with N-hydroxysuccinimide
437 ester-conjugated fluorescence dye (Cy5, cytiva, PF11A25001; Cy3, cytiva, PA13105) in
438 100 mM $NaHCO_3$ (pH 8.3) in PBS for 1 h at room temperature in the dark. Dye-
439 conjugated Fabs were collected using PD MiniTrap G-25 column (Cytiva, 28918004; pre-
440 equilibrated with PBS) and were concentrated to 1 mg/mL using a 10-kDa cutoff Amicon
441 Ultracell Centrifuge Filter Unit (Merck, UFC5010BK), and stored at 4°C in the dark.
442
443 **Morpholino oligonucleotide labeling**
444 Antisense morpholino oligo nucleotide was labeled as previously described (Sato *et al*.,
445 2019). In brief, 3′-primary amino-modified morpholino oligonucleotides specific for miR-
446 430 was reacted with N-hydroxysuccinimide ester-conjugated Cy3 in 0.1 M $NaHCO_3$ (pH
447 8.3) for 1 h at room temperature in the dark. After the reaction, Cy3-labeled morpholino
448 oligonucleotide was purified using a PD MiniTrap G-25 column.
449
450 **Synthesis of PEG_{750}-LANA-JF646 (JF646-LANA)**
451 Preparative high-performance liquid chromatography (HPLC) was conducted by using a
452 JASCO HPLC system equipped with a UV-2075 spectrometer (230 nm), PU-4086 pumps,
453 a DG-4580 degasser, and an MX-2080-32 mixer using a YMC-Triart C18 (20 mm I.D. ×
454 250 mm or 10 mm I.D. × 250 mm) column at 40°C with a gradient of acetonitrile in 0.1%
455 aqueous trifluoroacetic acid (TFA) at a flow rate of 10 or 3.5 mL/min. Analytical HPLC
456 was conducted by using a JASCO HPLC system equipped with a UV-2075 spectrometer,
457 PU-4180 pumps, a DG-4580 degasser, and an MX-2080-32 mixer, using a YMC-Triart

458 Phenyl C18 (4.6 mm I.D. × 150 mm) column with a linear gradient of 2%–90% acetonitrile
459 in 0.1% aqueous TFA over 3–15 min.
460 Poly(ethylene glycol) methyl ethers (Mn = 750) were purchased from Sigma-Aldrich
461 (#202495). All protected α-amino acids were purchased from Watanabe Chemical
462 Industries, Ltd. (Hiroshima, Japan) and Peptide Institute, Inc. (Osaka, Japan). NovaPEG
463 Rink amide resin was purchased from Merck KGaA, Co. Other chemicals were used as
464 received, unless otherwise stated.
465 The LANA peptide was synthesized on a solid phase using NovaPEG-Rink-amide-resin
466 (Fig. S7A). The Fmoc-amino acid was sequentially coupled using the DIC-HOBt method
467 in N,N-dimethylformamide (DMF; 3 equiv. each) for 60 min at room temperature after
468 removal of each Fmoc group with 20% piperidine-DMF for 10 min. The N-terminus was
469 capped with 20% acetic anhydride in CH_2Cl_2 for 5 min. The peptide was cleaved from
470 the resin by treatment with TFA in the presence of triisopropylsilane (TIPS) and H_2O
471 (95:2.5:2.5) for 90 min at room temperature, and then was concentrated under reduced
472 pressure, and precipitated with ether to obtain crude peptides, which were purified with
473 preparative HPLC (0% acetonitrile for 5 min, followed by a linear gradient of 0%–60%
474 acetonitrile over 30 min with a flow rate of 10 mL/min) to afford the product $LANA_{5\text{-}22}\text{-}N_3$
475 peptide (Fig. S7B) as white solids after lyophilization. 3,4,5-Tris(PEG_{750})-N-(prop-2-yn-1-
476 yl)benzamide was synthesized (Fig. S7C) following a previously described method
477 (Fujiwara *et al*., 2021).
478 To synthesize PEG_{750}-LANA (Fig. S7D), Cu-Tris[(1-benzyl-1H-1,2,3-triazol-4-
479 yl)methyl]amine (TBTA) solution in water:tBuOH (1:2, 150 μL; separately prepared by
480 mixing 24 mM $CuSO_4$ solution in water and 24 mM TBTA solution in tBuOH) was added
481 to a stirred solution of $LANA_{5\text{-}22}\text{-}N_3$ (10 mM in water, 72 μL, 720 pmol) and 3,4,5-

482 tris(PEG_{750})-N-(prop-2-yn-1-yl)benzamide (50 mM in tBuOH, 14.4 μL, 720 pmol). Then,
483 sodium ascorbate aqueous solution (100 mM, 60 μL, 6.00 μmol) was added, and the
484 mixture was stirred at room temperature for 22 h. Insoluble materials were removed by
485 filtration, and the filtrate was purified with preparative HPLC (0% acetonitrile for 3 min,
486 followed by a linear gradient of 0%–25% acetonitrile over 2 min, then a linear gradient of
487 25%–80% acetonitrile over 35 min with a flow rate of 3.5 mL/min) to produce PEG_{750}-
488 LANA; (Fig. S7E) after lyophilization.

489 To synthesize PEG_{750}-LANA-JF646 (Fig. S7F), 276 μL of DMF was added to a
490 stirred solution of PEG750-LANA (10 mM in water, 40 μL, 400 pmol) and Janelia Fluor
491 646, N-succinimidyl ester (TOCRIS, 10 mM in DMSO, 44 μL, 720 pmol). Then, 40 μL
492 saturated sodium hydrogen carbonate aqueous solution was added, and the mixture was
493 stirred at room temperature for 5 h. Insoluble materials were removed by filtration, and
494 the filtrate was purified with preparative HPLC (0% acetonitrile for 3 min, followed by a
495 linear gradient of 0%–25% acetonitrile over 2 min, then a linear gradient of 25%–80%
496 acetonitrile over 35 min with a flow rate of 3.5 mL/min) to produce PEG_{750}-LANA-JF646
497 (Fig. S7G) after lyophilization. The final product was analyzed by a MALDI-TOFMS (Fig.
498 S8, Shimadzu Biotech Axima ToF^2 spectrometer).

499

500 **mRNA synthesis**

501 To clone zebrafish genes, RNA was prepared from 24 hpf embryos using TRIzol reagent
502 (Ambion, 15596026). Zebrafish WT beta-actin (actin WT, GenBank Accession:
503 AF025305), Exp6 (GenBank Accession: BC044132), cofilin1 (GenBank Accession:
504 AY398323), and cofilin2 (GenBank Accession: AY398324) cDNA were amplified from the
505 embryo RNA using PrimeScript™ II High Fidelity One Step RT-polymerase chain

506 reaction (PCR) Kit (Takara, R026A) using the following primers: actin WT: (5'-
507 ATGGATGATGAAATTGCCGCACTGGTTGT-3') and (5'-
508 GAAGCATTTGCGGTGGACGATGGATGGTCC-3'); Exp6: (5'-
509 ATGGCGTCAGAGGAGGCCTCCTTACGGGCC-3') and (5'-
510 TAACTTCAGCGTTCCCGGCGGGAGGCTCCC-3'); cofilin1: (5'-
511 ATGGCCTCAGGTGTAGC-'3) and (5'-TTAGACAGGCTTCCCCTCC-'3); cofilin2 (5'-
512 ATGGCCTCCGGAGTTAC-3') and (5'-TCAATCGGTTAGAGGCTTTCC-3'). Amplified
513 cDNA was cloned into pSC plasmid (StrataClone Blunt PCR Cloning Kit, STRATAGENE,
514 240207). Then, the actin R62D mutant was obtained by inverse PCR using the following
515 primers (5'-GATGAGGCTCAGAGCAAGAGAGGTATCCTGACCCTGAAG-3') and (5'-
516 CTTCAGGGTCAGGATACCTCTCTTGCTCTGAGCCTCATC-3'). The nucleotide
517 sequence was validated by Sanger sequencing. For *in vitro* transcription, actin WT and
518 R62D were inserted into the EcoRI and NotI sites of the pcDNA3.1 + poly(A)83 plasmid
519 (Yamagata *et al*., 2005) with sfCherry or 3×FLAG-tag and NLS (see below). Exp6 was
520 inserted into the EcoRI and NotI sites of the pcDNA3.1 + poly(A)83 plasmid with
521 3×FLAG-tag. Cofilin1 or cofilin2 were inserted into the EcoRI and NotI sites of the
522 pcDNA3.1 + poly(A)83 plasmid with sfCherry and NLS. The resulting
523 pcDNA3.1_sfCherry-NLS + poly(A)83, pcDNA3.1_actin R62D-sfCherry-NLS + poly(A)83,
524 pcDNA3.1_actin WT-sfCherry-NLS + poly(A)83, pcDNA3.1_actin R62D-3×FLAG-NLS +
525 poly(A)83, pcDNA3.1_actin WT-3×FLAG-NLS + poly(A)83 pcDNA3.1_sfCherry-NLS +
526 poly(A)83, pcDNA3.1_Cofilin1-sfCherry-NLS + poly(A)83, pcDNA3.1_Cofilin2-sfCherry-
527 NLS + poly(A)83 were linearized by XbaI digestion, and pcDNA3.1_Exp6-3×FLAG-NLS
528 + poly(A)83 was linearized by XhoI digestion. The linearized plasmids were treated with
529 0.2 mg/mL proteinase K (Invitrogen, 25530-015), purified with phenol–chloroform

530 treatment and ethanol precipitation, then processed through *in vitro* transcription using
531 mMESSAGE mMACHINE T7 Transcription Kit (Ambion, AM1344) according to the
532 manufacturer's instruction. The concentration of synthesized mRNA was measured and
533 adjusted to 50, 250, 300, or 800 ng/μL by using nuclease-free water (Cytiva,
534 SH30538.01) containing 0.05% phenol red (SIGMA-ALDRICH, P5530-5G) as an
535 injection marker.
536
537 **Nuclear Localization Signal cloning**
538 Nucleoplasmin 2B (NPM, GenBank Accession: NM_001123007) was amplified from 24
539 hpf embryo RNA using the PrimeScript II High Fidelity One Step RT-PCR kit (Takara,
540 R026A) and the following primers; 5'-ATGAGCAAAACCGAGAAACC-3' and 5'-
541 TCACGCCTTCGCCTTC-3'. The nucleotide sequence was validated with Sanger
542 sequencing. NPM cDNA was fused to the C-terminus of sfGFP and cloned into pcDNA3.1
543 containing a poly(A) tail sequence for mRNA synthesis, as described above. After
544 confirming the nuclear localization of sfGFP-NPM, the potential NLS region containing
545 41 amino acids at the C-terminus was subcloned into the same vector. The 41 amino
546 acids directed sfGFP to the nuclei, so were used as an NLS in zebrafish embryos.
547
548 **Western blotting**
549 After dechorionation and injection, zebrafish embryos were incubated at 28°C for 5.3 h.
550 At the 50%-epiboly stage, the yolk was removed by hand using a pair of sharp forceps
551 and the cells were washed three times in 0.3× Danieau's buffer. Ten de-yolked embryos
552 were transferred into a 1.5 ml protein low bind-tube (Eppendorf, 0030108116) with the
553 buffer and the number of the embryos was confirmed under a stereoscopic microscope.

554 A gel-loading tip (QSP, 010-R204S-Q) was used to remove as much of the extra buffer
555 as possible. Then, 10 μL 2× SDS-gel loading buffer (125 mM Tris–HCl, 0.01%
556 bromophenol blue, 4% SDS, 20% glycerol, 100 mM DTT) was added to the embryos,
557 mixed by vortex and boiled at 95°C for 5 min. The 10 embryos were loaded into each
558 lane and separated on a 7.5% polyacrylamide gel (SuperSep Ace, FUJIFILM Wako Pure
559 Chemical, 191-14931), then transferred onto a polyvinylidene fluoride membrane (PALL,
560 BSP0161) using a semi-dry blotting system (ATTO). After blocking with Blocking-One
561 (Nacalai Tesque, 0395395), the membrane was incubated with anti-DYKDDDDK
562 antibody (1E6, 1 μg/mL, FUJIFILM Wako Pure Chemical, 012-22384) overnight at 4°C.
563 After washing with TBST (0.01% Tween-20, 10 mM Tris, 150 mM NaCl, pH 8.0), the
564 membrane was incubated with horseradish peroxidase-conjugated goat anti-Mouse IgG
565 (1:1000 dilution, Jackson ImmunoResearch, 115-035-146) overnight at 4°C. After
566 washing the membrane with TBST, the signal was developed using Western Lightning®
567 Plus-ECL (PerkinElmer, NEL104001EA) and detected using a gel documentation system
568 (ATTO, LuminoGraphII).
569
570 **Data analysis**
571 The intensity ratio of the nucleus to the cytoplasm depicted in Figs. 2, 3, 8C, S4, S5, and
572 S6 were measured as previously described (Sato *et al.*, 2019) using MATLAB software
573 (https://github.com/lhilbert/NucCyto_Ratio_TimeLapse). Using this code, the nuclear
574 area was segmented by the Cy5-labeled H3K9ac channel, and the cytoplasm was
575 defined as the region between 3.3 μm and 8.3 μm from the surface of the nucleus. To
576 measure the intensity ratio of the nucleus or chromosomes to the cytoplasm of UtrCH
577 shown in Fig.4C and 8B, a single z-section of the equatorial plane of each nucleus was

578 selected, and the nuclear area was determined based on the JF646- LANA or Hoechst
579 signal. The cytoplasmic area was defined as the region between 0.3 μm and 2.5 μm from
580 the edge of the nucleus using ImageJ FIJI (ver. 2.1.0).
581 Drawing line graphs, box plots, and statistical analyses were performed by using R
582 software (version 4.0.3; https://www.r-project.org/). The data distribution of each dataset
583 was first analyzed using Kolmogorov-Smirnov test. For parametric samples, the
584 homoscedasticity was analyzed using *F*-test, and then Student's *t*-test (unpaired, two-
585 tailed, Fig. 7A; comparing N/C ratio with homoscedasticity) was used.

586 **Acknowledgement**

587 We appreciate Mari Iwabuchi and Kazuo Yamagata for plasmids, Lennart Hilbert for
588 MatLab code, and Masahiko Harata, Kei Miyamoto and members in Kimura lab for
589 discussion. We thank the Biomaterials Analysis Division, Open Facility Center, Tokyo
590 Institute of Technology for DNA sequencing.

591

592 **Competing interests**

593 No competing interests declared.

594

595 **Funding**

596 This work was in part supported by Japan Society for the Promotion of Science KAKENHI
597 grants (JP17J06627 and JP21K15103 to H.O., JP17KK0143 and JP20K06484 to Y.S.,
598 JP21H02074 to S.A.K., JP20H00489 to M.K., and JP18H05527 and JP21H04764 to
599 H.K.), Japan Science and Technology CREST (JPMJCR20S6 to Y.S. and JPMJCR16G1
600 to H.K.), the Max Planck Society and the University of Lausanne (to N.L.V., M.P., and
601 E.W.), and Fonds de la Recherche en Santé du Québec (FRQS) postdoctoral fellowship
602 to E.W.

References

Amano, T., Kaji, N., Ohashi, K. and Mizuno, K. (2002). Mitosis-specific Activation of LIM Motif-containing Protein Kinase and Roles of Cofilin Phosphorylation and Dephosphorylation in Mitosis. *J. Biol. Chem.* 277, 22093–22102.

Baarlink, C., Wang, H. and Grosse, R. (2013). Nuclear actin network assembly by formins regulates the SRF coactivator MAL. *Science* 340, 864–867.

Baarlink, C., Plessner, M., Sherrard, A., Morita, K., Misu, S., Virant, D., Kleinschnitz, E.-M., Harniman, R., Alibhai, D., Baumeister, S., *et al*. (2017). A transient pool of nuclear F-actin at mitotic exit controls chromatin organization. *Nat. Cell Biol.* 19, 1389–1399.

Barbera, A.J., Chodaparambil, J.V., Kelley-Clarke, B., Joukov, V., Walter, J.C., Luger, K., and Kaye, K.M. (2006). The nucleosomal surface as a docking station for Kaposi's sarcoma herpesvirus LANA. *Science* 311, 856-861.

Belin, B. J., Lee, T. and Mullins, R. D. (2015). DNA damage induces nuclear actin filament assembly by Formin -2 and Spire-½ that promotes efficient DNA repair. *eLife* 4, e07735.

Bohnsack, M. T., Stüven, T., Kuhn, C., Cordes, V. C. and Görlich, D. (2006). A selective block of nuclear actin export stabilizes the giant nuclei of Xenopus oocytes. *Nat. Cell Biol.* 8, 257–263.

Brueckner, F. and Cramer, P. (2008). Structural basis of transcription inhibition by α-amanitin and implications for RNA polymerase II translocation. *Nat. Struct. Mol. Biol*. 15, 811–818.

Burkel, B. M., von Dassow, G. and Bement, W. M. (2007). Versatile fluorescent probes for actin filaments based on the actin-binding domain of utrophin. *Cell Motil. Cytoskeleton* 64, 822–832.

Caridi, C. P., Plessner, M., Grosse, R. and Chiolo, I. (2019). Nuclear actin filaments in DNA repair dynamics. *Nat. Cell Biol.* 21, 1068–1077.

Chin, S. M., Jansen, S. and Goode, B. L. (2016). TIRF microscopy analysis of human Cof1, Cof2, and ADF effects on actin filament severing and turnover. *J. Mol. Biol*. 428, 1604.

Chiolo, I., Minoda, A., Colmenares, S. U., Polyzos, A., Costes, S. V. and Karpen, G. H. (2011). Double-strand breaks in heterochromatin move outside of a dynamic HP1a domain to complete recombinational repair. *Cell,* 144, 732-744

Clark, T. G. and Merriam, R. W. (1977). Diffusible and bound actin in nuclei of *Xenopus laevis* oocytes. *Cell* 12, 883–891.

Clark, T. G. and Rosenbaum, J. L. (1979). An actin filament matrix in hand-isolated nuclei of X. *laevis* oocytes. *Cell* 18, 1101–1108.

Dancker, P., Löw, I., Hasselbach, W. and Wieland, T. (1975). Interaction of actin with phalloidin: Polymerization and stabilization of F-actin. *Biochim. Biophys. Acta - Protein Struct*. 400, 407–414.

Dopie, J., Skarp, K. P., Rajakylä, E. K., Tanhuanpää, K. and Vartiainen, M. K. (2012). Active maintenance of nuclear actin by importin 9 supports transcription. *Proc. Natl. Acad. Sci. U. S. A.* 109, E544-552

Dunkley, S., Scheffler, K. and Mogessie, B. (2022). Cytoskeletal form and function in mammalian oocytes and zygotes. *Curr. Opin. Cell Biol*. 75, 102073.

Farina, F., Gaillard, J., Guérin, C., Couté, Y., Sillibourne, J., Blanchoin, L. and Théry, M. (2016). The centrosome is an actin-organizing centre. *Nat. Cell Biol.* 18, 65–75.

Farina, F., Ramkumar, N., Brown, L., Samandar Eweis, D., Anstatt, J., Waring, T., Bithell, J., Scita, G., Thery, M., Blanchoin, L., *et al*. (2019). Local actin nucleation tunes centrosomal microtubule nucleation during passage through mitosis. *EMBO J*. 38, e99843.

Fujiwara, Y., Yamanashi, Y., Fujimura, A., Sato, Y., Kujirai, T., Kurumizaka, H., Kimura, H., Yamatsugu, K., Kawashima, S. A. and Kanai, M. (2021). Live-cell epigenome manipulation by synthetic histone acetylation catalyst system. *Proc. Natl. Acad. Sci*. 118, e2019554118.

Hadzhiev, Y., Qureshi, H. K., Wheatley, L., Cooper, L., Jasiulewicz, A., Van Nguyen, H., Wragg, J. W., Poovathumkadavil, D., Conic, S., Bajan, S., et al. (2019). A cell cycle-

coordinated Polymerase II transcription compartment encompasses gene expression before global genome activation. *Nat. Commun.* 2019 101 10, 1–14.

Hayashi-Takanaka, Y., Stasevich, T. J., Kurumizaka, H., Nozaki, N. and Kimura, H. (2014). Evaluation of chemical fluorescent dyes as a protein conjugation partner for live cell imaging. *PLoS One* 9, e106271.

Hayashi-Takanaka, Y., Yamagata, K., Wakayama, T., Stasevich, T. J., Kainuma, T., Tsurimoto, T., Tachibana, M., Shinkai, Y., Kurumizaka, H., Nozaki, N., *et al*. (2011). Tracking epigenetic histone modifications in single cells using Fab-based live endogenous modification labeling. *Nucleic Acids Res.* 39, 6475–6488.

Heyn, P., Kircher, M., Dahl, A., Kelso, J., Tomancak, P., Kalinka, A. T. and Neugebauer, K. M. (2014). The earliest transcribed zygotic genes are short, newly evolved, and different across species. *Cell Rep*. 6, 285–292.

Hofmann, W. A., Arduini, A., Nicol, S. M., Camacho, C. J., Lessard, J. L., Fuller-Pace, F. V and De Lanerolle, P. (2009). SUMOylation of nuclear actin. *J. Cell Biol*. 186, 193–200.

Ikegami, R., Zhang, J., Rivera-Bennetts, A. K. and Yager, T. D. (1997). Activation of the metaphase checkpoint and an apoptosis programme in the early zebrafish embryo, by treatment with the spindle-destabilising agent nocodazole. *Zygote* 5, 329–350.

Jevtić, P. and Levy, D. L. (2015). Nuclear size scaling during *Xenopus* early development contributes to midblastula transition timing. *Curr. Biol.* 25, 45–52.

Joseph, S. R., Pálfy, M., Hilbert, L., Kumar, M., Karschau, J., Zaburdaev, V., Shevchenko, A. and Vastenhouw, N. L. (2017). Competition between histone and transcription factor binding regulates the onset of transcription in zebrafish embryos. *eLife* 6, e23326

Kaji, N., Muramoto, A. and Mizuno, K. (2008). LIM Kinase-mediated Cofilin Phosphorylation during Mitosis Is Required for Precise Spindle Positioning. *J. Biol. Chem*. 283, 4983–4992.

Kane, D. A., Warga, R. M. and Kimmel, C. B. (1992). Mitotic domains in the early embryo of the zebrafish. *Nature* 360, 735–737.

Kane, D. A., Hammerschmidt, M., Mullins, M. C., Maischein, H. M., Brand, M., Van Eeden, F. J. M., Furutani-Seiki, M., Granato, M., Haffter, P., Heisenberg, C. P., *et al*. (1996). The zebrafish epiboly mutants. *Development* 123, 47–55.

Kimmel, C. B., Ballard, W. W., Kimmel, S. R., Ullmann, B. and Schilling, T. F. (1995). Stages of embryonic development of the zebrafish. *Dev. Dyn*. 203, 253–310.

Kimura, H. and Yamagata, K. (2015). *Nuclear Reprogramming*. (ed. Beaujean, N., Jammes, H., and Jouneau, A.), pp. 124-147, New York, NY: Springer New York.

Kita, A. M., Swider, Z. T., Erofeev, I., Halloran, M. C., Goryachev, A. B. and Bement, W. M. (2019). Spindle-F-actin interactions in mitotic spindles in an intact vertebrate epithelium. *Mol. Biol. Cell* 30, 1645–1654.

Lénárt, P., Bacher, C. P., Daigle, N., Hand, A. R., Eils, R., Terasaki, M. and Ellenberg, J. (2005). A contractile nuclear actin network drives chromosome congression in oocytes. *Nature* 436, 812–818.

Lucas, I., Chevrier-Miller, M., Sogo, J. M. and Hyrien, O. (2000). Mechanisms ensuring rapid and complete DNA replication despite random initiation in *Xenopus* early embryos. *J. Mol. Biol.* 29, 769-786

Mahbubani, H. M., Paull, T., Eider, J. K. and Blow, J. J. (1992). DNA replication initiates at multiple sites on plasmid DNA in *Xenopus* egg extracts. *Nucleic Acids Res.* 20, 1457–1462

Mathavan, S., Lee, S. G. P., Mak, A., Miller, L. D., Murthy, K. R. K., Govindarajan, K. R., Tong, Y., Wu, Y. L., Lam, S. H., Yang, H., *et al*. (2005). Transcriptome analysis of zebrafish embryogenesis using microarrays. *PLoS Genet*. 1, 0260–0276.

Misu, S., Takebayashi, M. and Miyamoto, K. (2017). Nuclear actin in development and transcriptional reprogramming. *Front. Genet*. 8, 27

Miyamoto, K., Pasque, V., Jullien, J. and Gurdon, J. B. (2011). Nuclear actin polymerization is required for transcriptional reprogramming of Oct4 by oocytes. *Genes Dev.* 25, 946–958.

Miyamoto, K., Teperek, M., Yusa, K., Allen, G. E., Bradshaw, C. R. and Gurdon, J. B. (2013). Nuclear Wave1 Is Required for Reprogramming Transcription in Oocytes and for Normal Development. *Science* 341, 1002–1005.

Mogessie, B. and Schuh, M. (2017). Actin protects mammalian eggs against chromosome segregation errors. *Science*. 357, eaal1647.

Mori, M., Monnier, N., Daigle, N., Bathe, M., Ellenberg, J. and Lénárt, P. (2011). Intracellular transport by an anchored homogeneously contracting F-actin meshwork. *Curr. Biol.* 21, 606–11.

Mori, M., Somogyi, K., Kondo, H., Monnier, N., Falk, H. J., Machado, P., Bathe, M., Nédélec, F. and Lénárt, P. (2014). An Arp2/3 nucleated F-actin shell fragments nuclear membranes at nuclear envelope breakdown in starfish oocytes. *Curr. Biol*. 24, 1421–8.

Murray, A. W. (1991). Xenopus laevis: Practical Uses in Cell and Molecular Biology. *Methods Cell Biol*. 36, 581–605.

Newport, J. and Kirschner, M. (1982). A major developmental transition in early *Xenopus* embryos: I. characterization and timing of cellular changes at the midblastula stage. *Cell* 30, 675–686.

Nguyen, V., Giannoni, F., Dubois, M.-F., Seo, S.-J., Vigneron, M., Kédinger, C. and Bensaude, O. (1996). In vivo degradation of RNA polymerase II largest subunit triggered by alpha-amanitin. *Nucleic Acids Res*. 24, 2924–2929.

Oda, H., Shirai, N., Ura, N., Ohsumi, K. and Iwabuchi, M. (2017). Chromatin tethering to the nuclear envelope by nuclear actin filaments: a novel role of the actin cytoskeleton in the *Xenopus* blastula. *Genes to Cells* 22, 376–391.

Okuno, T., Li, W. Y., Hatano, Y., Takasu, A., Sakamoto, Y., Yamamoto, M., Ikeda, Z., Shindo, T., Plessner, M., Morita, K., *et al*. (2020). Zygotic Nuclear F-Actin Safeguards Embryonic Development. *Cell Rep*. 31, 107824.

Pálfy, M., Joseph, S. R. and Vastenhouw, N. L. (2017). The timing of zygotic genome activation. *Curr. Opin. Genet. Dev.* 43, 53–60.

Parisis, N., Krasinska, L., Harker, B., Urbach, S., Rossignol, M., Camasses, A., Dewar, J., Morin, N. and Fisher, D. (2017). Initiation of DNA replication requires actin dynamics and formin activity. *EMBO J*. 36, 3212–3231.

Plessner, M., Knerr, J. and Grosse, R. (2019). Centrosomal Actin Assembly Is Required for Proper Mitotic Spindle Formation and Chromosome Congression. *iScience* 15, 274–281.

Posern, G., Sotiropoulos, A. and Treisman, R. (2002). Mutant Actins Demonstrate a Role for Unpolymerized Actin in Control of Transcription by Serum Response Factor. *Mol. Biol. Cell* 13, 4167–4178.

Riedl, J., Crevenna, A. H., Kessenbrock, K., Yu, J. H., Neukirchen, D., Bista, M., Bradke, F., Jenne, D., Holak, T. A., Werb, Z., *et al*. (2008). Lifeact: A versatile marker to visualize F-actin. *Nature Methods* 5, 605-607.

Rocchetti, A., Hawes, C. and Kriechbaumer, V. (2014). Fluorescent labelling of the actin cytoskeleton in plants using a cameloid antibody. *Plant Methods* 10, 12.

Roeles, J. and Tsiavaliaris, G. (2019). Actin-microtubule interplay coordinates spindle assembly in human oocytes. *Nat. Commun*. 10, 4651.

Sato, Y., Hilbert, L., Oda, H., Wan, Y., Heddleston, J. M., Chew, T.-L., Zaburdaev, V., Keller, P., Lionnet, T., Vastenhouw, N., *et al*. (2019). Histone H3K27 acetylation precedes active transcription during zebrafish zygotic genome activation as revealed by live-cell analysis. *Development* 146, dev179127.

Satoh, N. (1977). 'Metachronous' cleavage and initiation of gastrulation in amphibian embryos. *Dev. Growth Differ.* 19, 111–117.

Scheffler, K., Giannini, F., Lemonnier, T. and Mogessie, B. (2022). The prophase oocyte nucleus is a homeostatic G-actin buffer. *J. Cell Sci.* 135, jcs259807.

Schoenenberger, C. A., Buchmeier, S., Boerries, M., Sütterlin, R., Aebi, U. and Jockusch, B. M. (2005). Conformation-specific antibodies reveal distinct actin structures in the nucleus and the cytoplasm. *J. Struct. Biol*. 152, 157–168.

Sokolova, M., Moore, H. M., Prajapati, B., Dopie, J., Meriläinen, L., Honkanen, M., Matos, R. C., Poukkula, M., Hietakangas, V. and Vartiainen, M. K. (2018). Nuclear Actin Is Required for Transcription during Drosophila Oogenesis. *iScience* 9, 63-70.

Spencer, V. A., Costes, S., Inman, J. L., Xu, R., Chen, J., Hendzel, M. J. and Bissell, M. J. (2011). Depletion of nuclear actin is a key mediator of quiescence in epithelial cells. *J. Cell Sci*. 124, 123–132.

Spracklen, A. J., Fagan, T. N., Lovander, K. E. and Tootle, T. L. (2014). The pros and cons of common actin labeling tools for visualizing actin dynamics during Drosophila oogenesis. *Dev. Biol.* 393, 209–226.

Stüven, T., Hartmann, E. and Görlich, D. (2003). Exportin 6: A novel nuclear export receptor that is specific for profilin-actin complexes. *EMBO J.* 22, 5928–5940.

Tian, X., Qi, W., Chen, H., Zeng, X., Han, L. and Mi, D. (2016). β-Actin regulates interleukin 6-induced p21 transcription by interacting with the Rpb5 and Rpb7 subunits of RNA polymerase II. *Animal Cells and Systems* 20, 282-288.

Vartiainen, M. K., Guettler, S., Larijani, B. and Treisman, R. (2007). Nuclear actin regulates dynamic subcellular localization and activity of the SRF cofactor MAL. *Science* 316, 1749-1752.

Vartiainen, M. K., Mustonen, T., Mattila, P. K., Ojala, P. J., Thesleff, I., Partanen, J. and Lappalainen, P. (2002). The three mouse actin-depolymerizing factor/cofilins evolved to fulfill cell-type-specific requirements for actin dynamics. *Mol. Biol. Cell* 13, 183–194.

Vastenhouw, N. L., Cao, W. X. and Lipshitz, H. D. (2019). The maternal-to-zygotic transition revisited. *Development* 146, dev161471.

Wehland, J., Osborn, M. and Weber, K. (1977). Phalloidin-induced actin polymerization in the cytoplasm of cultured cells interferes with cell locomotion and growth. *Proc. Natl. Acad. Sci. U. S. A*. 74, 5613–7.

Wesolowska, N., Avilov, I., Machado, P., Geiss, C., Kondo, H., Mori, M. and Lénárt, P. (2020). Actin assembly ruptures the nuclear envelope by prying the lamina away from nuclear pores and nuclear membranes in starfish oocytes. *eLife* 9, e49774.

White, R. J., Collins, J. E., Sealy, I. M., Wali, N., Dooley, C. M., Digby, Z., Stemple, D. L., Murphy, D. N., Billis, K., Hourlier, T., *et al*. (2017). A high-resolution mRNA expression time course of embryonic development in zebrafish. *eLife* 6, e30860.

Wioland, H., Guichard, B., Senju, Y., Myram, S., Lappalainen, P., Jégou, A. and Romet-Lemonne, G. (2017). ADF/Cofilin Accelerates Actin Dynamics by Severing Filaments and Promoting Their Depolymerization at Both Ends. *Curr. Biol*. 27, 1956-1967.e7.

Woolner, S., O'Brien, L. L., Wiese, C. and Bement, W. M. (2008). Myosin-10 and actin filaments are essential for mitotic spindle function. *J. Cell Biol.* 182, 77–88.

Xu, Y. Z., Thuraisingam, T., De Lima Morais, D. A., Rola-Pleszczynski, M. and Radzioch, D. (2010). Nuclear translocation of β-actin is involved in transcriptional regulation during macrophage differentiation of HL-60 cells. *Mol. Biol. Cell* 21, 811–820.

Yamagata, K., Yamazaki, T., Yamashita, M., Hara, Y., Ogonuki, N. and Ogura, A. (2005). Noninvasive visualization of molecular events in the mammalian zygote. *Genesis* 43, 71–79.

603 **Figure legends**

604 **Figure 1. Nuclear F-actin in zebrafish early embryos detected by specific probes.**

605 (**A**-**C**) F-actin in fixed zebrafish embryos. Zebrafish embryos were fixed at the 32-, 128-,
606 1k-cell, and sphere stage, and stained with Acti-stain™ 555 phalloidin and Hoechst. Low
607 (**A**) and high (**B**) power views of single confocal sections are shown. (**C**) Relative intensity
608 profile plots of lines indicated in (**B**). The intensity is normalized using the average
609 cytoplasmic intensity. Phalloidin signals were clearly observed in nuclei of the 32-, 128-,
610 and 1k-cell stages. (**D**) F-actin in living zebrafish embryos. Zebrafish embryos were
611 injected with UtrCH-sfGFP as an F-actin probe and Cy5-labeled Fab for H3K9ac as a
612 chromatin marker. Every 90 s, 25 z-stack fluorescence images with 4 μm intervals were
613 acquired using a confocal microscope. Single z-sections are displayed. Accumulation of
614 UtrCH-sfGFP in nuclei is clearly observed in the 8- to the 1k-cell stage embryos
615 (arrowheads). Insets show the zoomed images of nuclei indicated by red arrowheads.
616 See also Movie 1. Scale bars: 50 μm (**A**), 10 μm (**B**), and 100 μm (**D**).

617

618 **Figure 2. Nuclear F-actin levels increased in the late interphase.**

619 Zebrafish embryos were injected with UtrCH-sfGFP and H3K9ac Fab-Cy5, and images
620 were acquired using the same procedure as described in Figure 1D. (**A**) Single confocal
621 sections of a nucleus in different cell stages are depicted with the time (min) after the
622 onset of the interphase. Scale bar: 20 μm. (**B**) The nucleus to cytoplasmic (N/C) intensity
623 ratios of UtrCH-sfGFP were measured. The mean values of UtrCH-sfGFP N/C ratios with
624 the standard deviations (s. d.) and the number of nuclei, as identified by H3K9ac Fab-
625 Cy5, are plotted. The duration of interphase is shaded in orange from the 8- to 1k-cell
626 stage. N/C ratios of UtrCH-sfGFP are above 1.0 (orange line) up to the 1k-cell stage.

627

628 **Figure 3. LifeAct-sfGFP accumulates in nuclei in early stage embryos.**

629 Zebrafish embryos were injected with LifeAct-sfGFP as an actin probe, H3S28ph Fab-
630 Cy3 as a mitotic chromosome marker, and H3K9ac Fab-Cy5 as a chromatin marker.
631 Every 90 s, 25 z-stack fluorescence images with 4 μm intervals were acquired using a
632 confocal microscope. (**A**) Single confocal sections of a nucleus at the 512-cell stage
633 (2.75 hpf) are shown. LifeAct-sfGFP accumulated in the nucleus up to 12 min and
634 disappeared at 13.5 min, when H3S28ph was observed on condensed chromosomes.
635 Scale bar: 20 μm. (**B**) Mean values of N/C ratios are plotted with standard deviations (s.
636 d.). The duration of interphase is shaded in orange from the 8- to 1k-cell stage. N/C ratios
637 of LifeAct-sfGFP are above 1.0 (orange line) up to the 1k-cell stage. (**C**) Interphase nuclei
638 were selected based on a low H3S28ph Fab signal (N/C ratio <2.2). The numbers of
639 nuclei with different ranges of LifeAct-sfGFP N/C ratio in every time point are plotted as
640 cumulative bars. After the 1k-cell stage, the number of nuclei with LifeAct-sfGFP N/C
641 ratio <1.0 increased.

642

643 **Figure 4. F-actin that accumulated in the nucleus remained there after nuclear**
644 **envelope breakdown (NEBD).**

645 Zebrafish embryos were injected with UtrCH-sfGFP as an F-actin probe, TMR-labeled
646 155-kDa dextran to monitor NEBD, and JF646-LANA as a chromatin marker. Every 12.5
647 s, confocal sections were acquired during the 1k-cell (**A**) and the high (**B**) stages. UtrCH-
648 sfGFP accumulated in nuclei (**A** and **B**, −37.5 s to −12.5 s) and remained in the vicinity
649 of chromosomes even after NEBD (**A** and **B**, 0 s to 37.5 s). (**C**) Nucleus/Cytoplasm or
650 Chromosome area/Cytoplasm intensity ratio of UtrCH-sfGFP and TMR-Dextran were

651 measured (N = 10) at the 512-cell, 1k-cell, and high stages. The mean values were
652 shown with the s. d. Nuclear actin levels increased at the late interphase to prophase
653 (from −50 s to 0 s) with a peak at around NEBD (0 s). After NEBD, UtrCH-sfGFP gradually
654 decreased from chromatin (from 0 s to 50 s) during the prometaphase. Scale bars: 20
655 μm.
656
657 **Figure 5. Actin patches remained in the vicinity of chromosomes during**
658 **prometaphase and disappeared at the metaphase in the 1k-cell stage embryos.**
659 Zebrafish embryos were injected with UtrCH-sfGFP, TMR-tubulin, and JF646-LANA.
660 Every 15 s, confocal sections were acquired. (**A**) Single sections of UtrCH-sfGFP, TMR-
661 tubulin, and JF646-LANA at the 1k-cell stage embryo, and their merged and magnified
662 images are shown. Relative intensity profile plots of lines are indicated at the bottom.
663 The intensity is normalized using maximum and minimum intensity. UtrCH-sfGFP signals
664 are located by chromosomes. (**B**) The surface rendering three-dimensional images are
665 shown (green: UtrCH-sfGFP, magenta: JF646-LANA, cyan: TMR-Tubulin). UtrCH-sfGFP
666 accumulated in the nucleus (−15 s) remained in the vicinity of condensing chromosomes
667 after NEBD (from 0 s to 45 s) and disappeared before the chromosomes were aligned at
668 the metaphase (60 s). Just after NEBD (0 s and 15 s), TMR-Tubulin does not appear to
669 reach chromosomes when UtrCH-sfGFP patches are around. When UtrCH-sfGFP
670 patches partially disappear (15 s and 30 s), TMR-Tubulin appears to capture condensing
671 chromosomes (15 s and 30 s). See also Movie 4. Scale bars: 20 μm. See Figure S3 for
672 the sphere stage.
673
674 **Figure 6. Actin patches partially remained in the vicinity of chromosomes during**

675 **prometaphase and disappeared at the metaphase in the high stage embryos.**

676 Zebrafish embryos were injected with UtrCH-sfGFP, TMR-tubulin, and JF646-LANA.
677 Every 15 s, confocal sections were acquired. (**A**) Single sections of UtrCH-sfGFP, TMR-
678 tubulin, and JF646-LANA at the high stage embryo, and their merged and magnified
679 images are shown. Relative intensity profile plots of lines are indicated at the bottom.
680 The intensity is normalized using maximum and minimum intensity. UtrCH-sfGFP signals
681 are located in the vicinity of chromosomes. (**B**) The surface rendering three-dimensional
682 images are shown (green: UtrCH-sfGFP, magenta: JF646-LANA, cyan: TMR-Tubulin).
683 UtrCH-sfGFP signals appeared around condensing chromosomes after NEBD (from 0 s
684 to 45 s) and disappeared before the chromosomes were aligned at the metaphase (60
685 s). Just after NEBD (0 s and 15 s), TMR-Tubulin does not appear to reach chromosomes
686 associated with UtrCH-sfGFP patches. TMR-Tubulin appears to capture condensing
687 chromosomes (0 s to 30 s). See also Movie 5. Scale bars: 20 μm.

688

689 **Figure 7. Actin patches appeared during prophase to prometaphase and**
690 **disappeared at the metaphase in the sphere stage embryo.**

691 Zebrafish embryos were injected with UtrCH-sfGFP, TMR-labeled tubulin, and JF646-
692 LANA. Every 15 s, confocal sections were acquired. (**A**) Single sections for UtrCH-sfGFP,
693 TMR-labeled tubulin, and JF646-LANA in sphere stage embryo, and their merged and
694 magnified images are shown. (**B**) The surface rendering three-dimensional images are
695 shown (green: UtrCH-sfGFP, magenta: JF646-LANA, cyan: TMR-Tubulin). Weak UtrCH-
696 sfGFP signals were observed in the vicinity of chromosomes after NEBD (0 s and 15 s)
697 and disappeared (45 s) before chromosomes aligned at the metaphase (60 s). Scale
698 bars: 20 μm.

699

700 **Figure 8. Transcription inhibition delayed the nuclear actin decrease after the 1k-**
701 **cell stage.**

702 (**A**) Zebrafish embryos were injected with α-amanitin to inhibit RNA-polymerase II-
703 mediated transcription, or the vehicle (PBS), with Cy3-labeled morpholino antisense
704 oligonucleotide for miR-430 transcripts as a transcription marker, and JF646-LANA as a
705 chromatin marker. Every 90 s, 25 z-stack images with 4 μm intervals were acquired using
706 a confocal microscope. 7 slices at each time point from the 128-cell to dome stage were
707 depicted and the max intensity projection images are shown. (**B**) Embryos were grown
708 to the 1k-cell stage and oblong stage before fixation and staining with Hoechst and Acti-
709 stain™ 555 phalloidin. Single confocal sections are shown with N/C ratios of phalloidin
710 intensity (N = 10). In the box plots, center lines show the medians; box limits indicate the
711 25th and 75th percentiles; whiskers extend 1.5 times the interquartile range from the
712 25th to 75th percentiles; × indicates the means; and data points are plotted as closed
713 circles (PBS, blue; α-amanitin, orange). *p*-values obtained with a Students *t*-test
714 (unpaired, two-tailed) are also shown (*, $p < 0.05$). At the 1k-cell stage, clear phalloidin
715 signals are observed in the nuclei of both embryos treated without or with α-amanitin. At
716 the oblong stage, phalloidin signals are not concentrated in the nucleus of embryos
717 without α-amanitin but are still observed in the nucleus of α-amanitin-treated embryos.
718 (**C**) Zebrafish embryos were injected with α-amanitin, or PBS, and then with UtrCH-
719 sfGFP and H3K9ac Fab-Cy5. Every 90 s, 25 z-stack fluorescence images with 4 μm
720 intervals were acquired. The mean values of N/C ratios (control: blue, +α-amanitin:
721 orange) are plotted with the s. d. from the 128-cell to dome stage. α-amanitin-injected
722 embryos showed the higher N/C ratio of UtrCH-sfGFP value in later stages (sphere and

723 dome). Single confocal sections at the sphere stage are shown on the right. UtrCH-
724 sfGFP remained accumulated in some nuclei during the sphere stage (orange
725 arrowheads). Scale bars: 10 μm (**A**) and 20 μm (**B** and **C**).

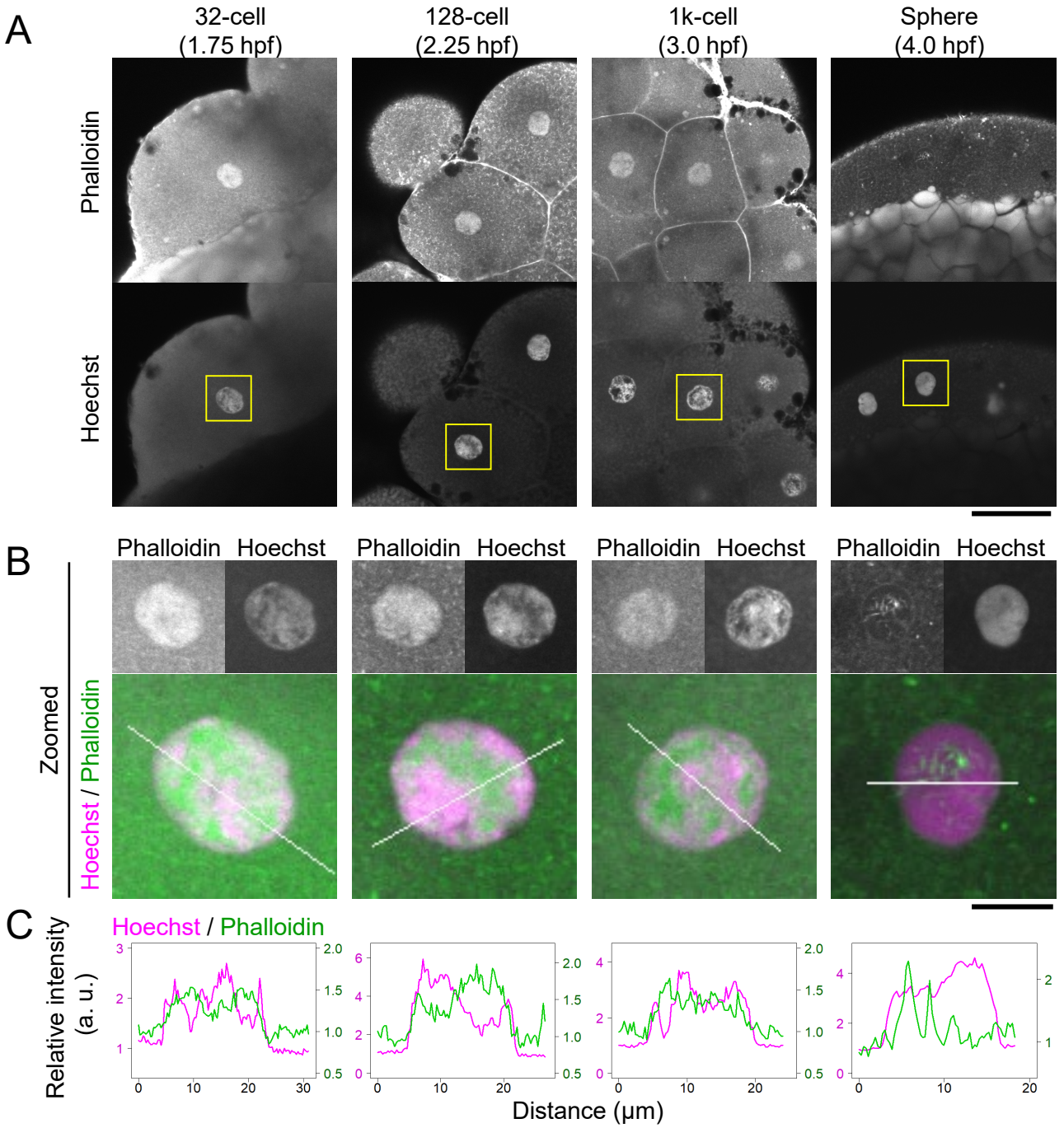
A
32-cell
(1.75 hpf)
128-cell
(2.25 hpf)
1k-cell
(3.0 hpf)
Sphere
(4.0 hpf)
Phalloidin
Hoechst
B
Phalloidin
Hoechst
Zoomed
Hoechst / Phalloidin
C
Hoechst / Phalloidin
Relative intensity
(a. u.)
Distance (μm)

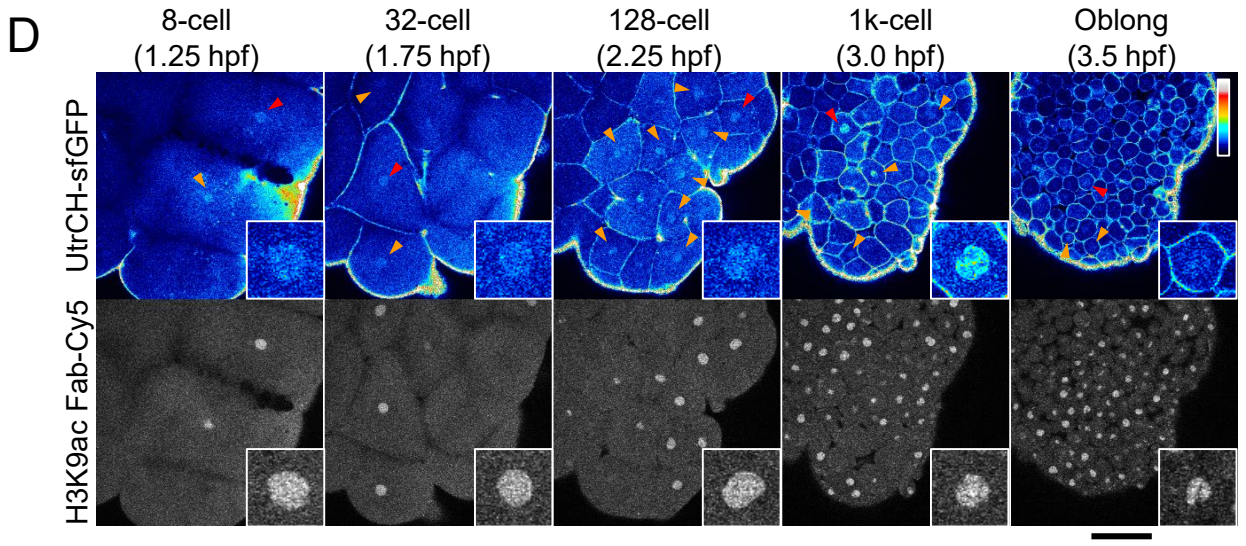
D
8-cell
(1.25 hpf)
32-cell
(1.75 hpf)
128-cell
(2.25 hpf)
1k-cell
(3.0 hpf)
Oblong
(3.5 hpf)
UtrCH-sfGFP
H3K9ac Fab-Cy5

Figure 1

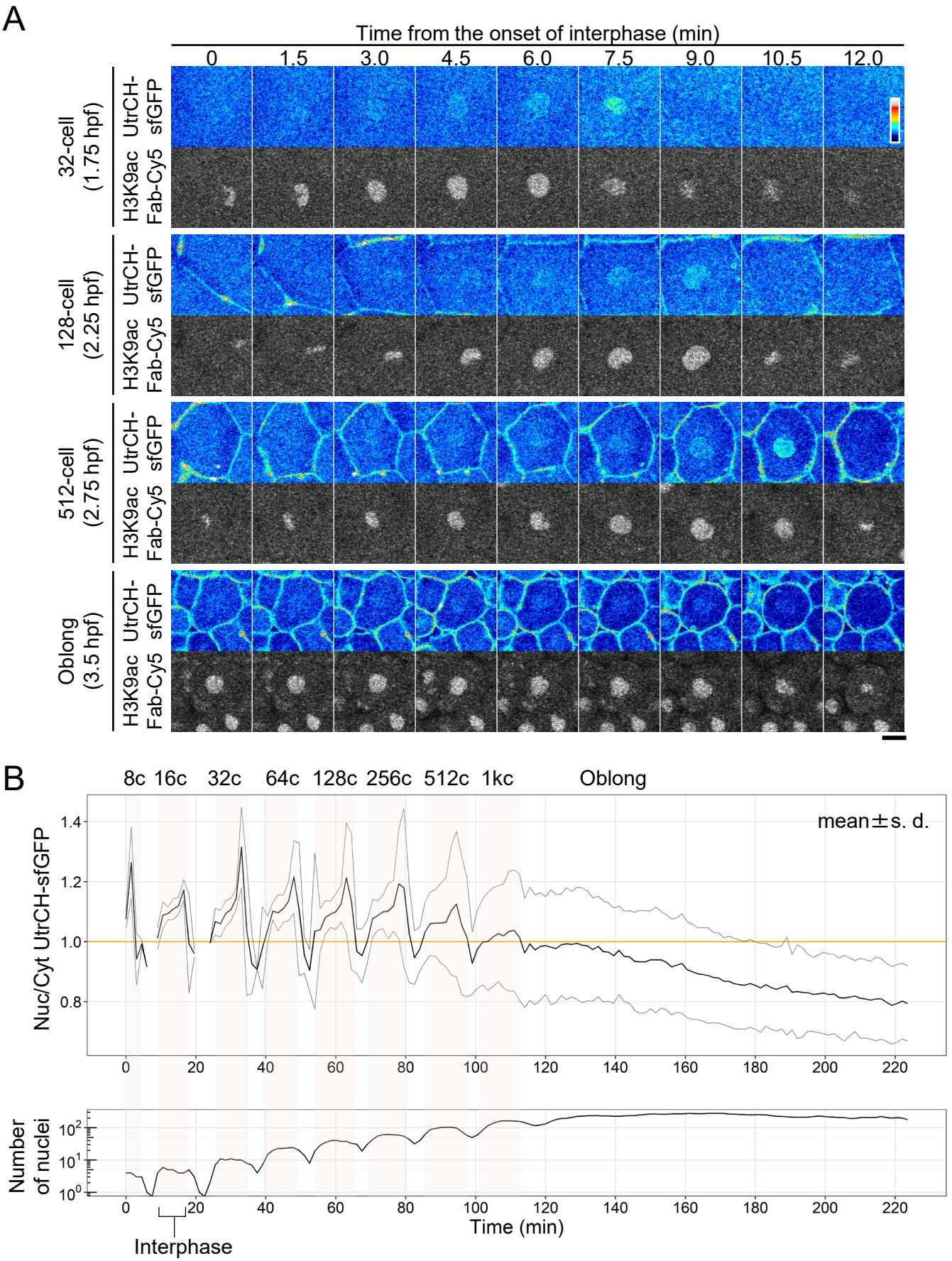
A
Time from the onset of interphase (min)
0
1.5
3.0
4.5
6.0
7.5
9.0
10.5
12.0
32-cell (1.75 hpf)
128-cell (2.25 hpf)
512-cell (2.75 hpf)
Oblong (3.5 hpf)
UtrCH-sfGFP
H3K9ac Fab-Cy5
B
8c
16c
32c
64c
128c
256c
512c
1kc
Oblong
mean±s. d.
Nuc/Cyt UtrCH-sfGFP
Number of nuclei
Time (min)
Interphase

Figure 2

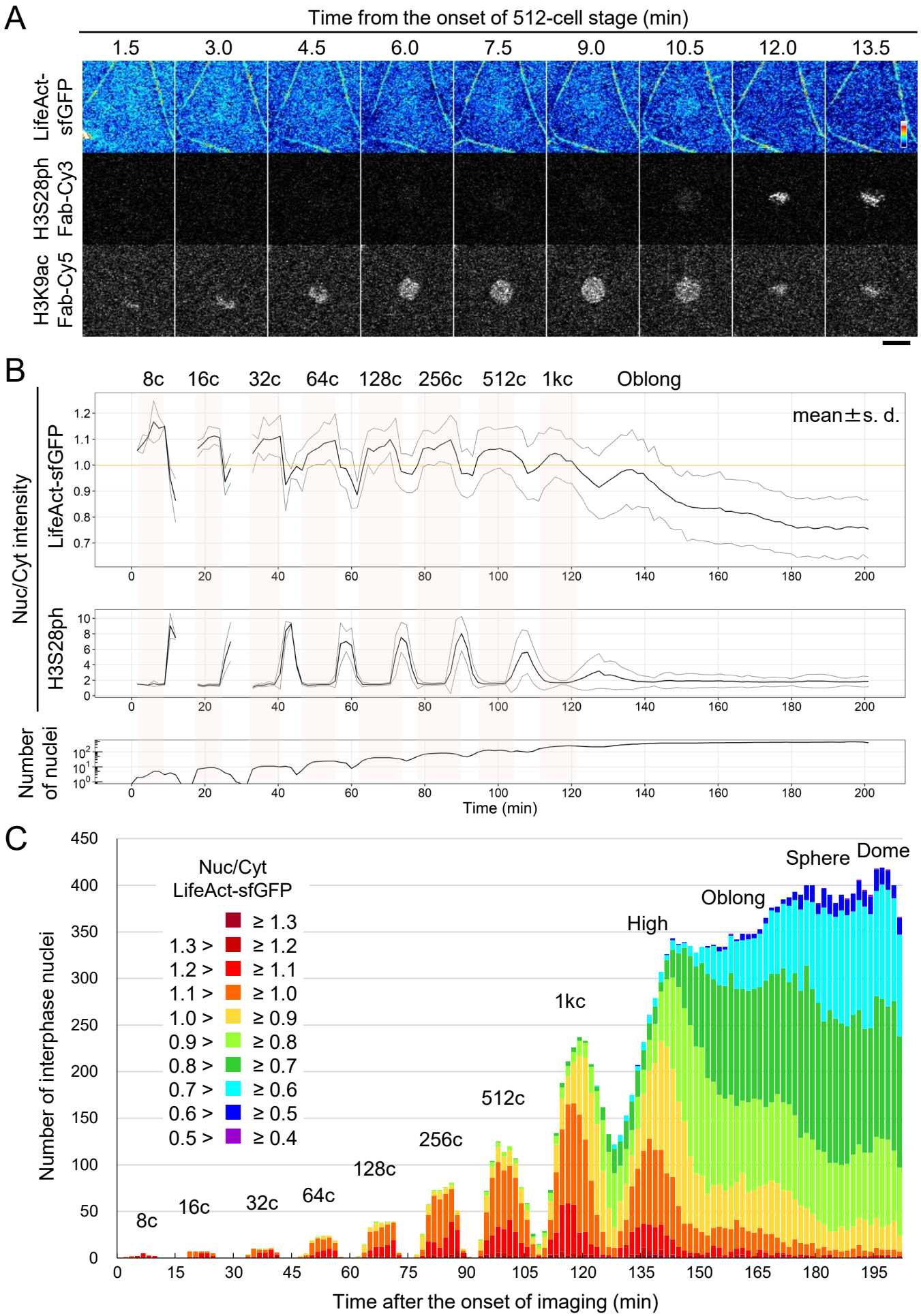
A
Time from the onset of 512-cell stage (min)
1.5
3.0
4.5
6.0
7.5
9.0
10.5
12.0
13.5
LifeAct-sfGFP
H3S28ph Fab-Cy3
H3K9ac Fab-Cy5
B
8c
16c
32c
64c
128c
256c
512c
1kc
Oblong
mean±s. d.
Nuc/Cyt intensity
LifeAct-sfGFP
H3S28ph
Number of nuclei
Time (min)
C
Nuc/Cyt LifeAct-sfGFP
≥ 1.3
1.3 > ≥ 1.2
1.2 > ≥ 1.1
1.1 > ≥ 1.0
1.0 > ≥ 0.9
0.9 > ≥ 0.8
0.8 > ≥ 0.7
0.7 > ≥ 0.6
0.6 > ≥ 0.5
0.5 > ≥ 0.4
Number of interphase nuclei
Time after the onset of imaging (min)
Sphere
Dome
Oblong
High
1kc
512c
256c
128c
64c
32c
16c
8c

Figure 3

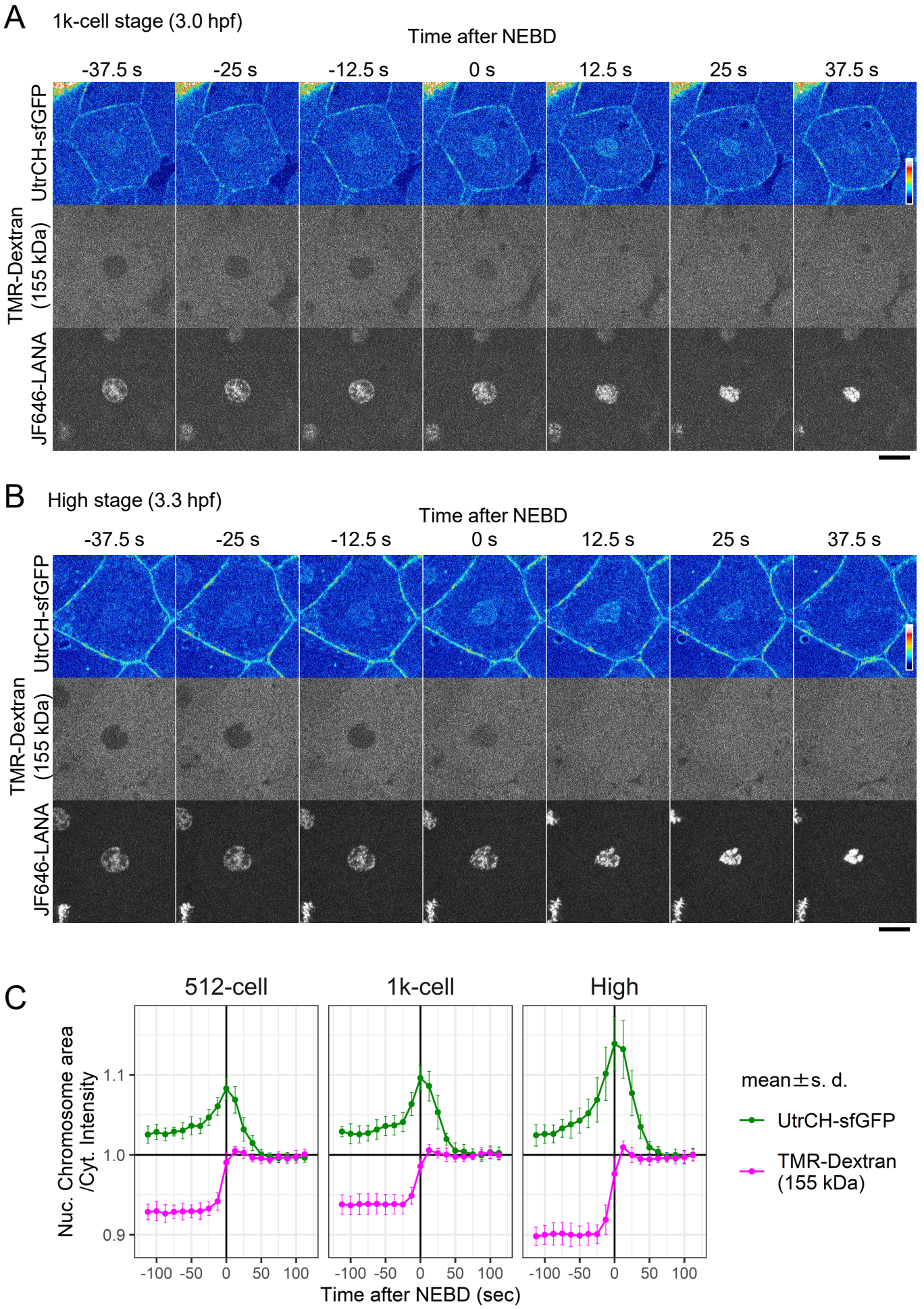
A
1k-cell stage (3.0 hpf)
Time after NEBD
-37.5 s
-25 s
-12.5 s
0 s
12.5 s
25 s
37.5 s
UtrCH-sfGFP
TMR-Dextran (155 kDa)
JF646-LANA
B
High stage (3.3 hpf)
Time after NEBD
-37.5 s
-25 s
-12.5 s
0 s
12.5 s
25 s
37.5 s
UtrCH-sfGFP
TMR-Dextran (155 kDa)
JF646-LANA
C
512-cell
1k-cell
High
Nuc. Chromosome area /Cyt. Intensity
1.1
1.0
0.9
-100 -50 0 50 100
Time after NEBD (sec)
mean±s. d.
UtrCH-sfGFP
TMR-Dextran (155 kDa)

Figure 4

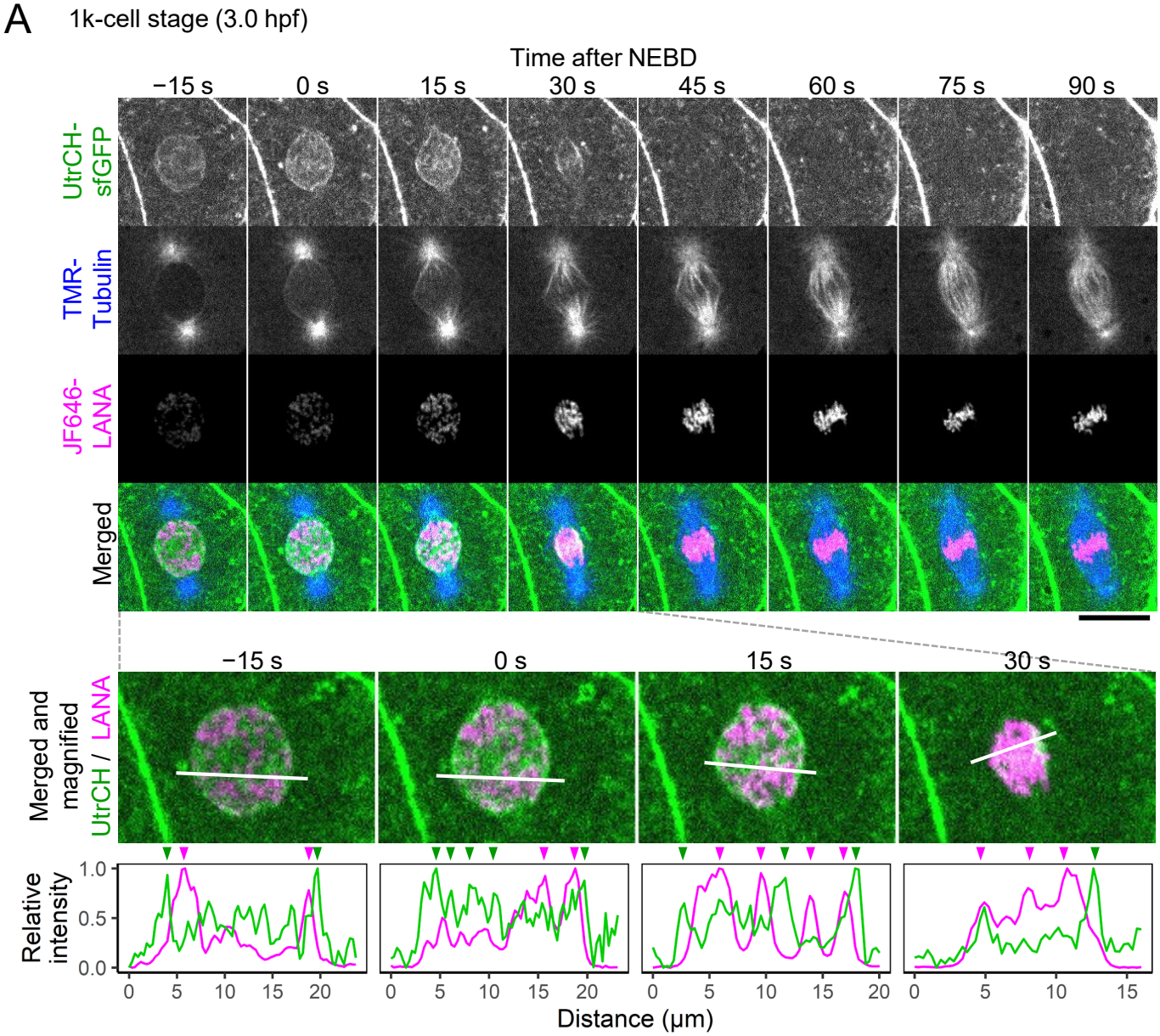
A
1k-cell stage (3.0 hpf)
Time after NEBD
−15 s
0 s
15 s
30 s
45 s
60 s
75 s
90 s
UtrCH-sfGFP
TMR-Tubulin
JF646-LANA
Merged
Merged and magnified
UtrCH / LANA
Relative intensity
1.0
0.5
0.0
0
5
10
15
20
Distance (μm)

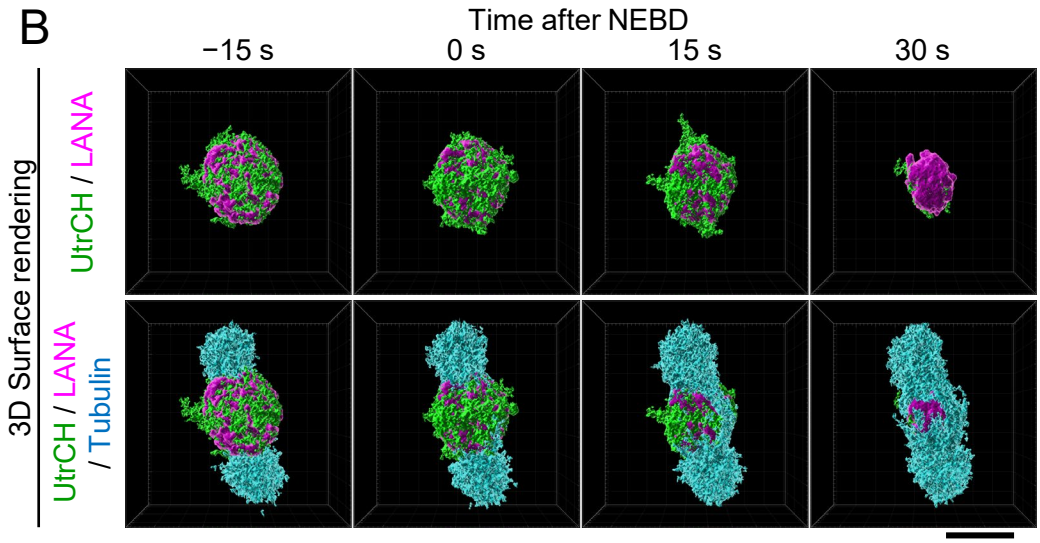
B
Time after NEBD
−15 s
0 s
15 s
30 s
3D Surface rendering
UtrCH / LANA
UtrCH / LANA / Tubulin

Figure 5

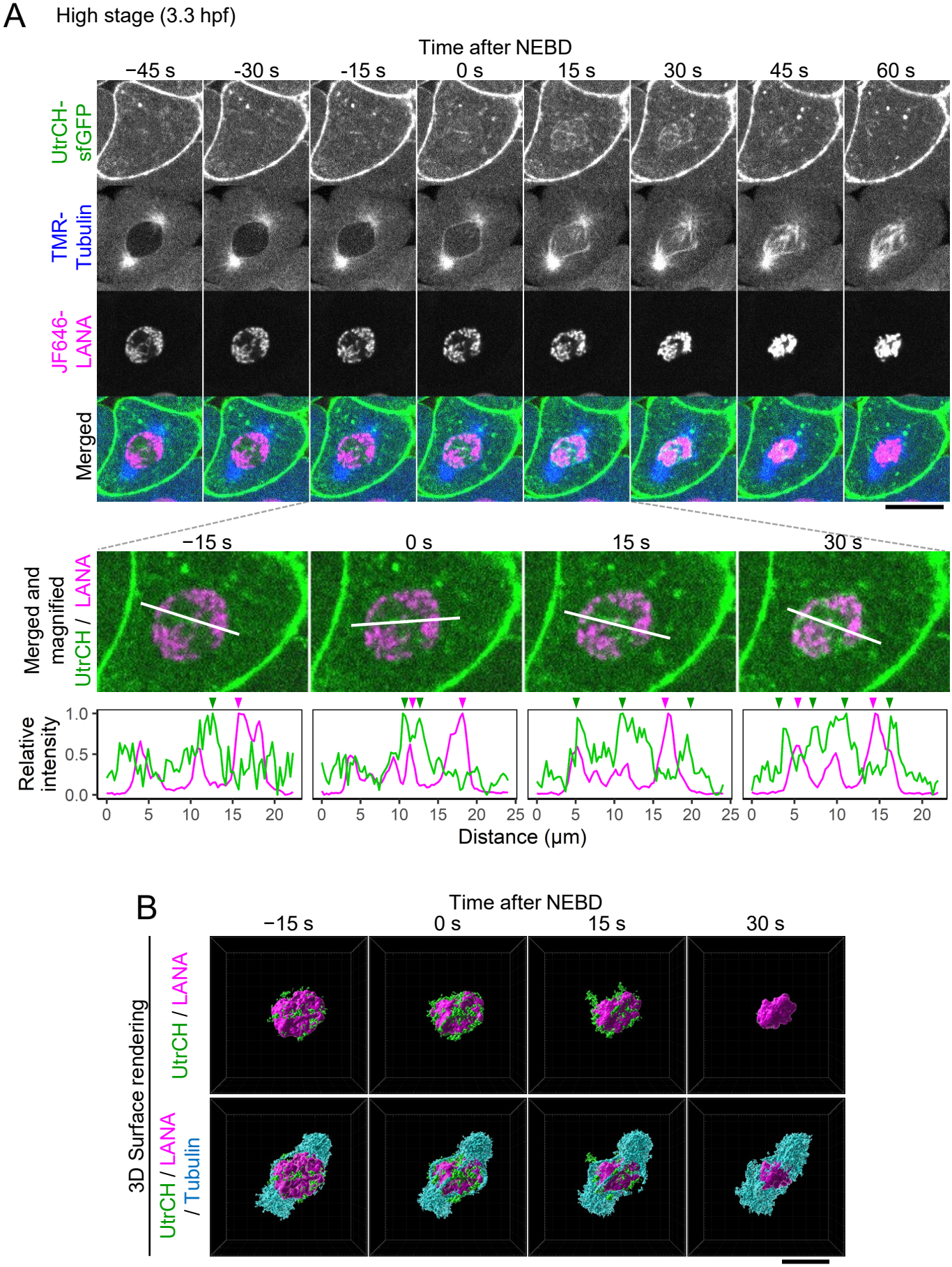
A
High stage (3.3 hpf)
Time after NEBD
−45 s
-30 s
-15 s
0 s
15 s
30 s
45 s
60 s
UtrCH-sfGFP
TMR-Tubulin
JF646-LANA
Merged
−15 s
0 s
15 s
30 s
Merged and magnified
UtrCH / LANA
Relative intensity
1.0
0.5
0.0
0
5
10
15
20
25
Distance (μm)
B
Time after NEBD
−15 s
0 s
15 s
30 s
3D Surface rendering
UtrCH / LANA
UtrCH / LANA / Tubulin

Figure 6

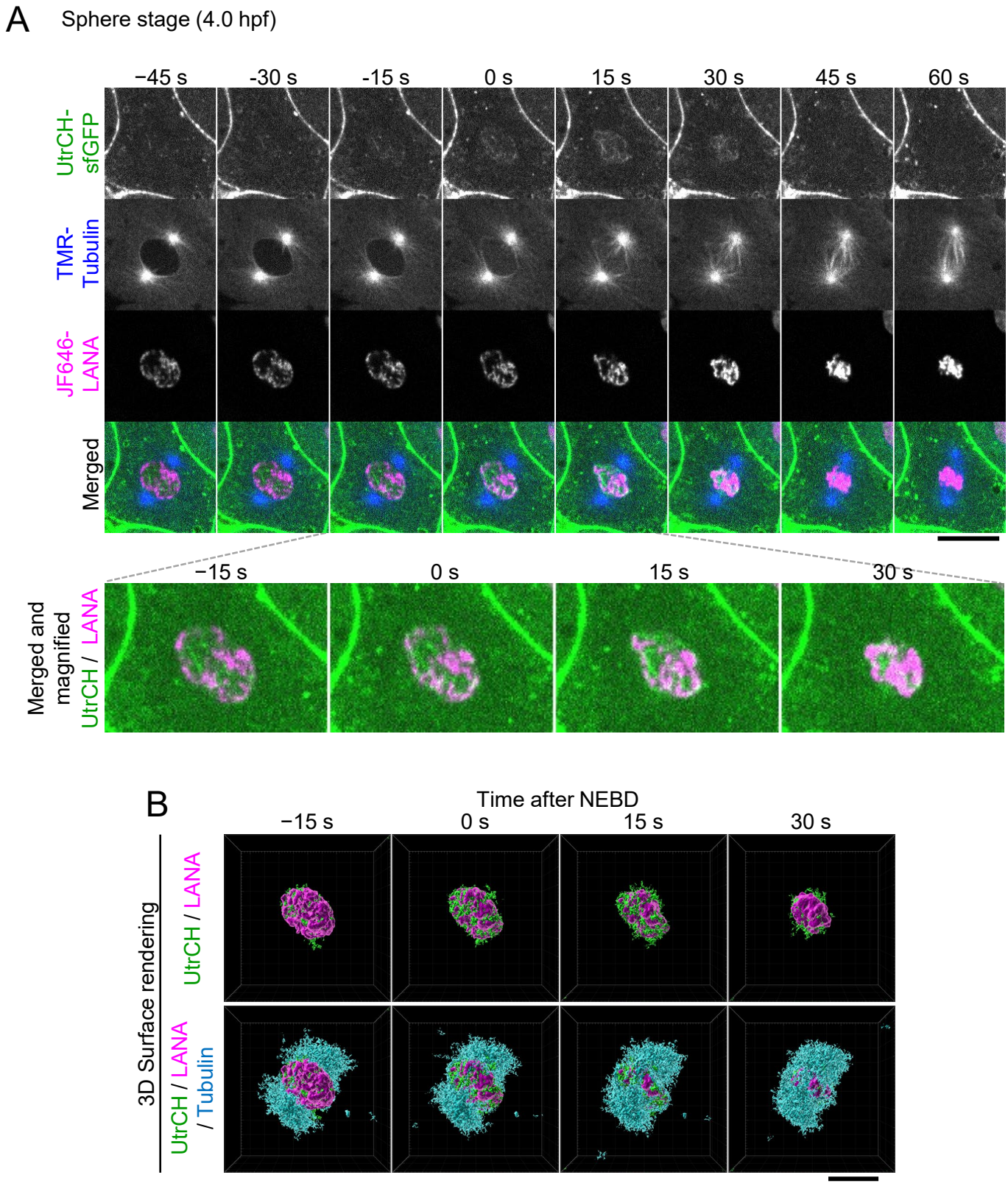
A
Sphere stage (4.0 hpf)
−45 s
-30 s
-15 s
0 s
15 s
30 s
45 s
60 s
UtrCH-sfGFP
TMR-Tubulin
JF646-LANA
Merged
−15 s
0 s
15 s
30 s
Merged and magnified
UtrCH / LANA
B
Time after NEBD
−15 s
0 s
15 s
30 s
3D Surface rendering
UtrCH / LANA
UtrCH / LANA / Tubulin

Figure 7

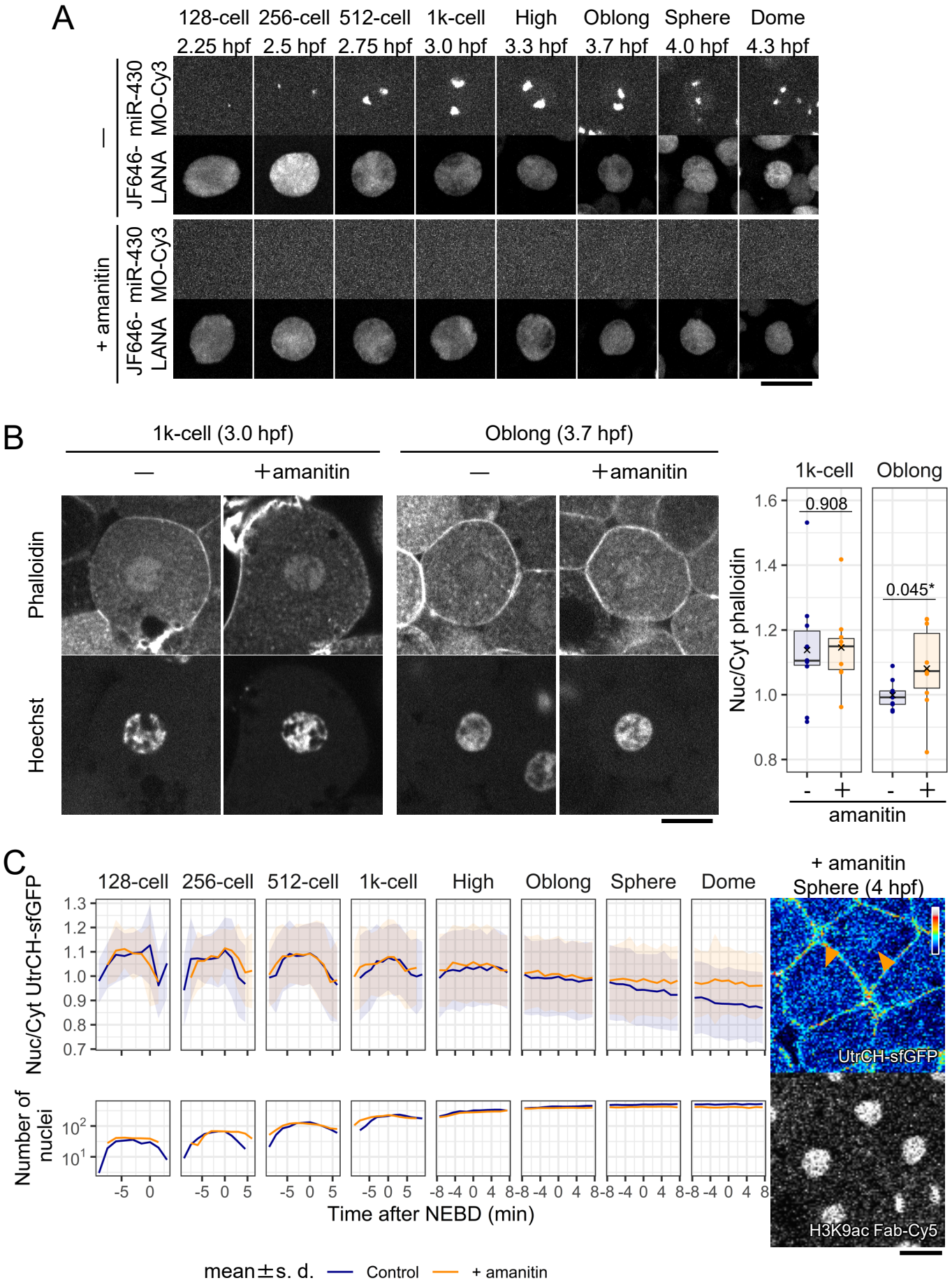
A
128-cell 2.25 hpf
256-cell 2.5 hpf
512-cell 2.75 hpf
1k-cell 3.0 hpf
High 3.3 hpf
Oblong 3.7 hpf
Sphere 4.0 hpf
Dome 4.3 hpf
—
+ amanitin
miR-430 MO-Cy3
JF646-LANA
B
1k-cell (3.0 hpf)
Oblong (3.7 hpf)
—
+amanitin
Phalloidin
Hoechst
1k-cell
Oblong
Nuc/Cyt phalloidin
0.908
0.045*
amanitin
C
128-cell
256-cell
512-cell
1k-cell
High
Oblong
Sphere
Dome
Nuc/Cyt UtrCH-sfGFP
Number of nuclei
Time after NEBD (min)
+ amanitin
Sphere (4 hpf)
UtrCH-sfGFP
H3K9ac Fab-Cy5
mean±s. d.
Control
+ amanitin

Figure 8